Title

Highly Uniform Colloidal Metasurfaces for the Photoluminescent Enhancement of Quantum Dot Active Layers

Permalink

https://escholarship.org/uc/item/592887dq

Author

Brown, Eric Raymer

Publication Date

2016

Peer reviewed|Thesis/dissertation

UNIVERSITY OF CALIFORNIA, SAN DIEGO

Highly Uniform Colloidal Metasurfaces for the Photoluminescent Enhancement of
Quantum Dot Active Layers

A Thesis submitted in partial satisfaction of the requirements for the degree Master of
Science

in

Nanoengineering

by

Eric Raymer Brown

Committee in charge:

      Professor Andrea R. Tao, Chair
      Professor Darren J. Lipomi
      Professor Donald J. Sirbuly

2016

The Thesis of Eric Raymer Brown is approved and it is acceptable in quality and form for publication on microfilm and electronically:

_____

_____

_____

Chair

University of California, San Diego

2016

TABLE OF CONTENTS

LIST OF FIGURES

LIST OF TABLES

LIST OF EQUATIONS

ACKNOWLEDGEMENTS

I would like to acknowledge Professor Andrea R. Tao for her support as chair of my committee. Her guidance over the past few years has been invaluable, and her passion for scientific discovery nothing short of inspirational.

I would also like to acknowledge Matthew J. Rozin, my colleague and friend, without whom this project would not have been possible. Through the many struggles with tricky fabrication and temperamental instrumentation, his assistance and guidance has been of immeasurable helpfulness for the past few years. It is easy to say that this project may have gone much differently without his partnership.

Chapters 3, 4, and 5, in part are currently being prepared for submission for publication of the material. Rozin, Matthew J,; Brown, Eric R.; Tao, Andrea R. The thesis author was one of the primary investigators and authors of this material.

ABSTRACT OF THE THESIS

Highly Uniform Colloidal Metasurfaces for the Photoluminescent Enhancement of

Quantum Dot Active Layers

by

Eric Raymer Brown

Master of Science of Nanoengineering

University of California, San Diego, 2016

Professor Andrea R. Tao, Chair

Colloidal metasurfaces are two-dimensional arrays of subwavelength resonators
generally composed of a precious metal substrate and a deposited layer of colloidal
metal nanoparticles, ultimately yielding a functional nanomaterial surface with a total
thickness on the order of 100 nanometers. Colloidal metasurfaces, like other

metasurfaces, possess the ability to control and manipulate light in ways that cannot be done using natural materials, yet have the added benefit of much faster, cheaper, and larger scale construction. The precise construction parameters of these colloidal metasurfaces allow for the tuning of an extreme, in-plane electromagnetic coupling phenomenon that is primarily localized within the metasurface "gap." Placing active materials (such as nanocrystals, fluorophores, and others) into this gap can lead to a variety of interesting effects that are potentially useful for the construction of larger functional devices. Certain types of active materials have very poor absorption capabilities, making them very difficult and/or inefficient to use as sensing agents and light collectors. Here we show that these colloidal metasurface gaps can be use to enhance the single- and multi-photon absorption efficiencies and subsequent emission intensities of an active layer of semiconducting nanocrystals via the integration of these nanocrystals into the metasurface gap during the metasurface construction process. Colloidal metasurfaces used for active layer enhancement can subsequently be tuned to accommodate many different types of absorbing active layers.

CHAPTER 1: INTRODUCTION

1.1 Basics of Plasmonic Nanoparticles

Surface plasmon resonance is a material phenomenon that occurs in certain transition metals, in which incident electromagnetic waves induce the oscillation of the free surface electrons of a transition metal by causing the formation of localized electronic dipoles within the material (Figure 1.1). When particles of these transition metals are confined to dimensions on the nanoscale, these plasmon resonances (referred to as Localized Surface Plasmon Resonances, or LSPRs) can cause the particles to show absorbance, scattering, and coupling properties based on their shapes and relative positions that are not seen within a bulk metal. These particles can then be incorporated into larger functional structures to yield a variety of electronic and optical effects that stem from plasmonic interactions.
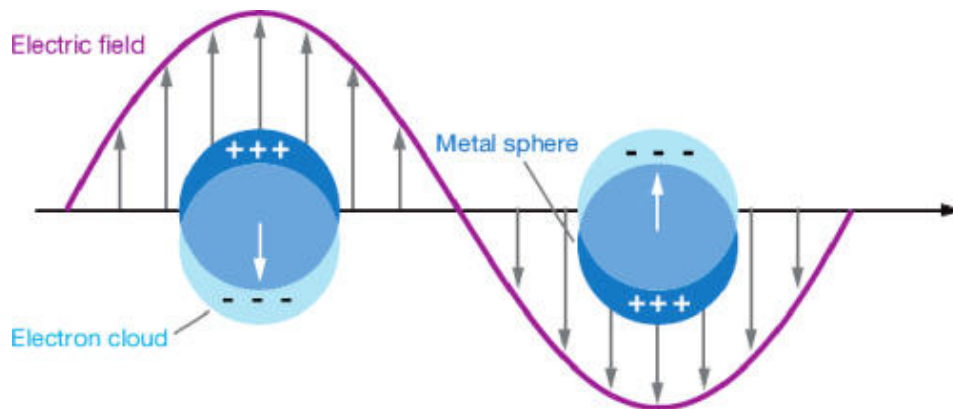
Figure 1.1 The induction of localized electronic dipole moments within spherical transition metal nanoparticles due to the coupling of incident EM radiation with the free surface electrons.[1]

Plasmonic nanoparticles (NPs) have become an important area of nanomaterial study due to their ability to localize light far below the scale of its natural wavelength, while simultaneously generating intense, localized electric fields in their immediately

surrounding regions.[1] Silver nanoparticles are of great interest specifically because silver

is an excellent conductor, is relatively non-reactive (compared to lithium and copper),

and has a very strong surface plasmon response that lies within the range of the visible

spectrum; additionally, they are far cheaper to produce than gold, platinum, or other

precious metal nanoparticles. Silver nanoparticles can also be manufactured into various

different individual geometries (Figure 1.2) depending on synthesis parameters, each of

which has a unique optical response that can be utilized to achieve different device

properties.[2]
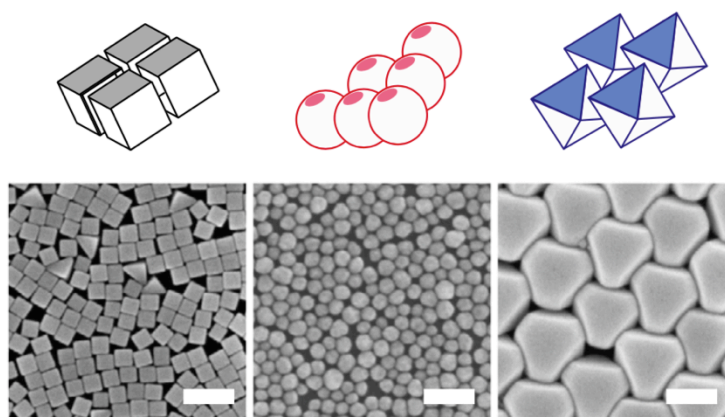
Figure 1.2 SEM images showing (from left to right) silver nanocubes, nanospheres, and nanooctahedra. Scale bars = 200 nm. The above corresponding diagrams show their respective packing structures when incorporated into a close-packed film as well as their contact areas with the underlying substrate.[3]

The particle used throughout these experiments was the silver nanocube

(AgNC), due to the fact that its relatively large contact area leads to a very strong LSPR

effect within the region between the cubes and their underlying substrate. Silver

nanocubes can be synthesized by a variety of different methods, including citrate

reduction, silver mirror reactions, polyol processes, seed-mediated growth, template-

directed growth, and lithographic fabrication methods.[2] However, many of these methods

are slow (15-26 hours in some cases)[4] and/or low-yield processes with limited capacities

for production on a manufacturing scale. The colloidal polyol synthesis process is comparatively fast and high yield. It involves the reduction of a silver salt precursor by viscous organic solvents containing more than one hydroxyl group (such as 1,5-pentanediol, 1,2-propylene glycol or ethylene glycol), while a polymeric ligand "capping-agent" such as polyvinylpyrrolidone (PVP) forces crystal formation into a cubic structure in a way that is uniform across every particle (Figure 1.3).[5,6] The polyol synthesis process was the preferred method of AgNC synthesis throughout this group of experiments.

$$2\ HO(CH_2)_5OH + O_2 \rightarrow 2\ HO(CH_2)_4CHO + 2H_2O$$
$$HO(CH_2)_4CHO + 2\ AgNO_3 \rightarrow 2Ag + 2\ HNO_3 + CH_3CO(CH_2)COCH_3$$
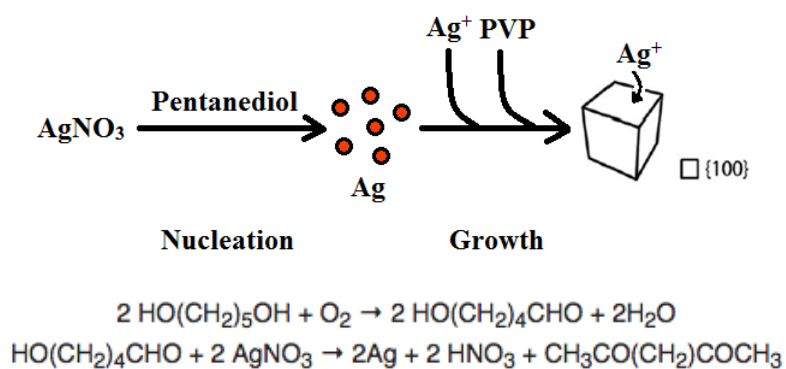
Figure 1.3 Schematic showing the basic progression of the silver nanocube polyol synthesis process, along with the redox reaction equation for the silver salt reduction.[6]

1.2 Basics of Colloidal Metasurfaces

Colloidal metasurfaces are two-dimensional arrays of sub-wavelength resonators generally composed of a precious metal substrate and a deposited layer of colloidal metal nanoparticles, ultimately yielding a functional nanomaterial surface that is flexible and conformal with a total thickness on the order of 100 nanometers. These surfaces have the capacity to control the flow of light in ways that are otherwise unattainable with natural materials,[3] and can be used to generate interesting optical effects when constructed using different active layer materials. Many of the unique properties

exhibited by colloidal metasurface structures are due to the formation of an LSPR cavity between the metal colloid (a silver nanocube in this case) lattice and the underlying metal substrate, as seen in Figure 1.4.[7,8] This is known as out-of-plane coupling, which refers to the interactions between the nanoparticle and the underlying metal film; the opposite of this is in-plane coupling, which refers to the interactions between particles on the surface. Light incident on this metasurface structure creates regions of highly intense light confinement within this LSPR cavity (also known as a "resonance gap"), which resonates at a characteristic wavelength. This characteristic resonance wavelength can be tuned by controlling the degree of both out-of-plane and in-plane coupling exhibited by the metasurface, which is typically done by manipulating several different parameters of device construction.[3,8] The degree to which these surfaces can be tuned as well as methods to do so will be discussed in Chapter 3.
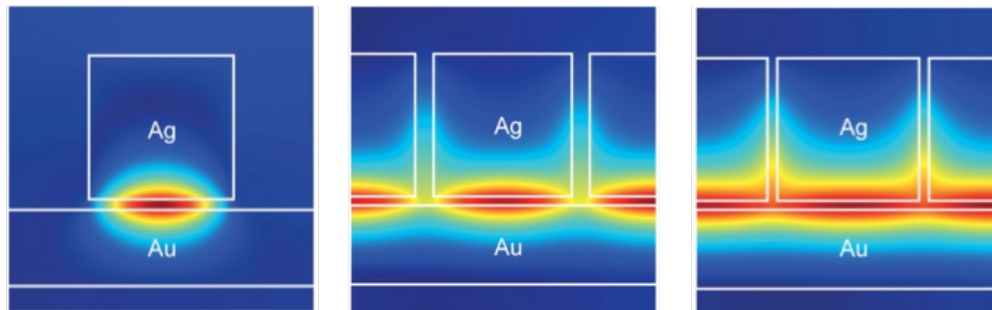
Figure 1.4 A two-dimensional schematic showing the resonance cavities formed by out-of-plane coupling between a silver nanocube and gold substrate for various nanocube planar densities.[3] Magnetic field strength is observed to be highest in the region directly between the nanocube face and the material surface. Higher nanocube densities typically lead to longer resonance wavelengths.

1.3 Incorporation of an Active Layer Material

One class of active material that can be incorporated into this plasmonic gap space is fluorescent entities, such as fluorophore dyes or semiconductor quantum dots (QDs). These materials, particularly quantum dots, are commonly used for applications such as sensing,[9-11] tagging,[9,12-13] and photonics.[9,14-15] They possess unique absorptive and emissive properties that can be manipulated by controlling their surrounding environment, most notably by placing them in proximity to plasmonic structures. The following work primarily examines the enhancement of the single- and multi-photon emissive properties of cadmium selenide (CdSe) QDs by placing them within a colloidal metasurface structure such that they are subject to the LSPRs that reside within the gap of the metasurface. A general schematic of this metasurface can be seen in Figure 1.5.
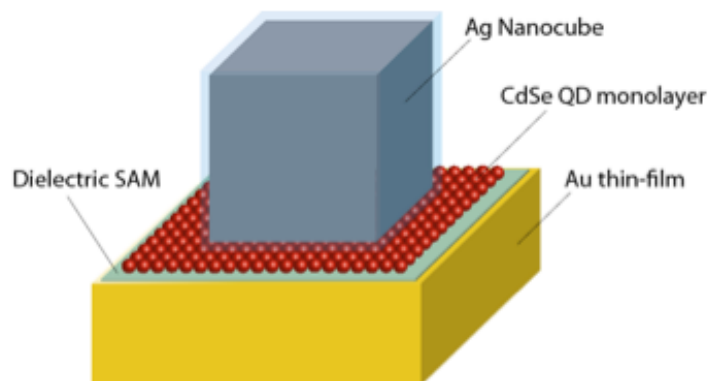
Figure 1.5 Schematic illustrating a single repeating unit of the colloidal metasurface structure with CdSe quantum dots incorporated into the metasurface gap. The overall thickness of the surface is on the order of 100 nm.

The general idea is that the placement of QDs within the resonance cavity in this structure will cause a dramatic increase in quantum yield for both single- and multi-photon emission events compared to QDs suspended in solution or on/within a more

simple type of two-dimensional structure. This use of this colloidal metasurface structure

possesses an advantage over most other types plasmonic layered materials due to its

relative ease of manufacturing and tuning flexibility, which allows for much easier

incorporation of active materials as well as potential for large-scale production.

CHAPTER 2: LAYERED NANOPARTICLE MATERIALS

2.1 What are Layered Materials?

Layered materials are a class of thin-film materials in which function is strictly governed by the ability to controllably interact with local environment in a well-defined manner. They are typically assembled using five distinct forms of "layer-by-layer" deposition techniques, which include immersive, spin, spray, electromagnetic, and fluidic assembly techniques.[16] Many of the specific techniques that fit into these five categories involve the sequential deposition of a colloidal solution, generally composed of entities such as proteins, macromolecules, or nanoparticles, onto a parent substrate to achieve some kind of ultimate functionality in the form of a controlled surface. Many layers of colloidal solution are often deposited onto one substrate to form more complex layered structures with correspondingly more complex physical, electronic, optical, or chemical properties.

2.2 Top-Down Methods for Assembling Nanoparticles

Before nanoparticle layers can be constructed into more complex layered surfaces, the individual nanoparticles themselves must often be assembled into well-ordered arrays or films with fairly homogenous particle densities. Particle density uniformity, much like other characteristics such as chemical composition and surface morphology, has a large effect on the overall properties of a layered surface or finished device. For this reason, a uniform particle layer is often desired in order to achieve consistent properties across an entire surface. Methods for assembling nanoparticles are generally divided into two major categories: top-down assembly and bottom-up assembly. A few examples of top-down methods will be discussed in this section.

One such top-down method for controllably assembling repeating arrays of nanoparticles is a form of nanosphere lithography (NSL) that involves reactive ion etching and thermal annealing.[17] Nanosphere lithography (Figure 2.1) involves depositing a layer of approximately 300 nm diameter polystyrene or silicon dioxide spheres somewhat randomly onto a substrate, which then assemble into localized, hexagonally-packed regions due to a combination of interparticle and external forces.[18] Metal is then deposited atop this layer of spheres, which then settles into the interstitial spaces between the packed spheres. The spheres are then washed away and the substrate annealed at high temperature to reveal a highly periodic array of spheroidal metal nanoparticles. However, NSL and other methods like voltage-pulse scanning probe lithography[19] and lift-off ion beam lithography[20] only "assemble" nanoparticles in the sense that they create periodic arrays of nanoscale features that are simply nanoparticle-esc. They typically exhibit a high degree of pattern fidelity, but are generally limited to creating poorly defined spheroidal particles with high levels of shape and size dispersity. The fabrication steps that they involve are also somewhat destructive in nature, meaning that these techniques cannot be used to make layered structures very effectively.
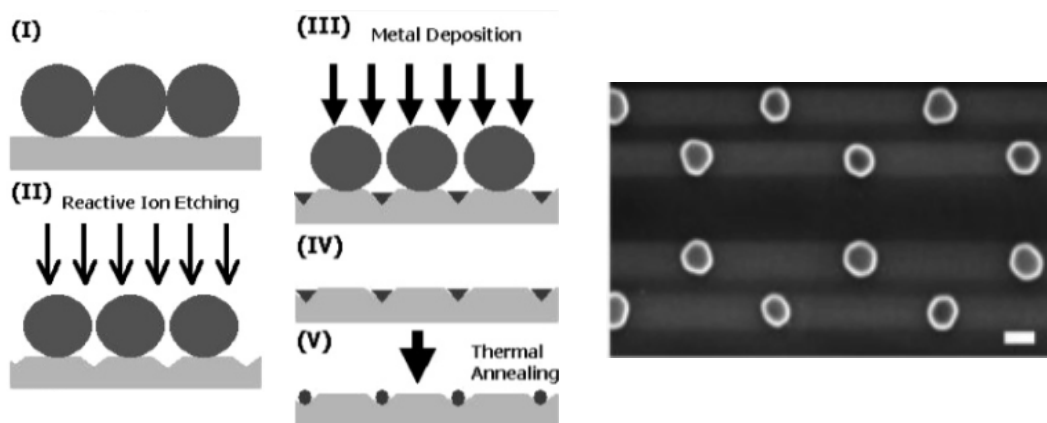
Figure 2.1 Schematic and accompanying SEM image demonstrating NP assembly with NSL. Scale bar = 200 nm.[17]

The limitations that apply to NSL, scanning probe lithography, and ion beam lithography also apply to most types of top-down approaches to creating patterned "nanoparticle" surfaces, and have spurred the recent development of processes that use colloidally synthesized nanoparticle solutions to fabricate repeating arrays. Electrospraying is one method that incorporates colloidally synthesized nanoparticle solutions into a top-down process in order to create assembled arrays of nanoparticles. Electrospraying[21] involves placing a suspension of nanoparticles (usually ranging from 10 – 100 nm in diameter) are placed into a non-reactive charging chamber; this chamber is usually some form of stainless steel capillary connected to a DC high-voltage supplier, which can control the charge of the suspended nanoparticles by the application of a positive or negative voltage of several kilovolts. A substrate is then "charge patterned" using a charged stainless steel needle (Figure 2.2) in a way that will attract the charged nanoparticles to localized areas. Either nitrogen (for positively charged NPs) or carbon dioxide (for negatively charged NPs) is then forced through the capillary and a nozzle, which then sprays the charged nanoparticles onto the patterned surface, resulting in a collection of nanoparticles at the oppositely charged regions (Figure 7).
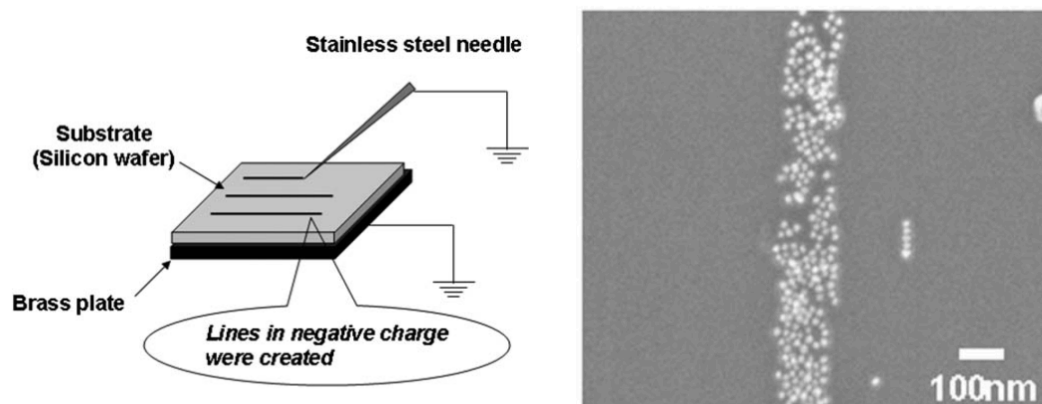
Figure 2.2 Schematic showing the substrate patterning procedure for the Electrospraying method (left) and a resultant electrosprayed nanoparticle pattern on a substrate surface (right).[21]

A third example of top-down nanoparticle assembly is microtransfer printing (μTP),[22] which utilizes conventional methods of photolithography and flexible polymeric stamps to deposit NPs onto substrates in a highly controlled manner (Figure 2.3).
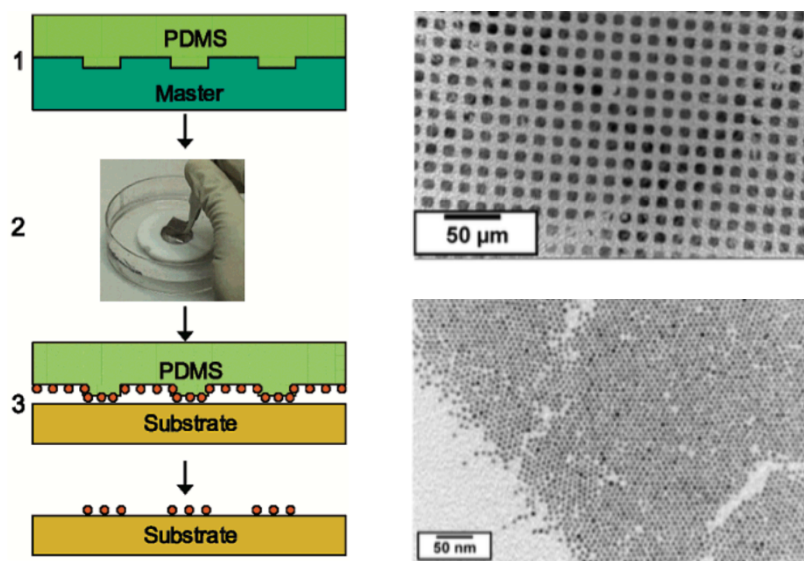
Figure 2.3 Schematic detailing the μCP process as well as accompanying SEM images showing resultant patterns.[22] Pattern uniformity is high on a large scale, but decreases at higher levels of magnification.

A master mold is first made from hard material (usually Si) using conventional photolithographic means. A viscous polymer resin, such as polydimethylsiloxane (PDMS), is poured over the mold and allowed to cure; upon removal, the cured polymer stamp retains the negative features of the master mold. A colloidal solution of nanoparticles is then suspended on an air-water interface using a Langmuir-Schaefer deposition technique to create a nanoparticle film on the water surface. The PDMS stamp is then lowered through this interface parallel to the orientation of the film, causing a transfer of nanoparticles from the water surface onto the surface of the PDMS stamp. Finally, this stamp is then pressed onto a separate substrate, leaving nanoparticles behind in the same pattern as that of the PDMS stamp. The μTP method is a very simple

and highly repeatable method that produces nanoparticle arrays with very high accuracy and also has the potential to be used to fabricate layered structures. The major disadvantage of µTP, as well as of most top-down methods, is that the ultimate resolution of the assembled nanoparticle patterns is greatly limited by the resolution capabilities of the top down processes. For example, the finest features possible using µTP are limited by the limits of conventional lithography. The inherent limits of top-down processes have generated interest in bottom-up assembly processes, which take advantage of interparticle interactions and chemical surface modification schemes to cause nanoparticles to assemble into highly periodic systems with a much higher degree of small-scale control possible than that of top-down processes.

2.3 Bottom-Up Methods for Assembling Nanoparticles

When concerning bottom-up nanoparticle assembly, the concept of "self-assembly" is often discussed. Self-assembly (SA) refers to the process by which nanoparticles, molecules, or other discrete entities spontaneously organize themselves due to direct specific interactions (such as interparticle forces) and/or indirectly due to environmental conditions (such as external fields).[23] An exhaustive discussion of all common methods for the bottom-up self-assembly of nanoparticles would be unwieldy and inappropriate for this work, so a few selected relevant examples will be discussed in this section.

Externally directed SA generally refers to self-assembly methods that use external fields or apparatus to control nanoparticle assembly and ordering. Electric and magnetic fields are commonly used to induce interactions between particles in a suspension or medium.[23] Most nanoparticles will polarize when placed within electric fields, due to the mismatch between the dielectric properties of the particle and the

medium.[24] Mobile charges that form the electrostatic double layer surrounding

nanoparticle surfaces[25] also interact with applied electric fields and can contribute to the

overall polarization of the nanoparticle.[26] The practical upshot of this is that many

parameters of electric and magnetic fields can be manipulated to assemble colloidal

nanoparticles into even larger parent structures, such as electrically functional

microwires (Figure 2.4).[23,27] However, the use of electrical and magnetic fields to control

particle assembly is generally limited by the ability to control the fields themselves, which

is often very difficult and imprecise.
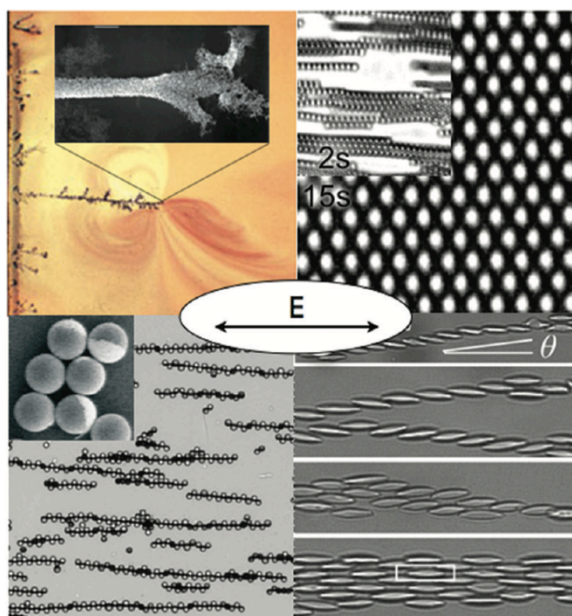
Figure 2.4 Figure showing example structures fabricated by the direct assembly of nanoparticles in external fields.[23] Top left: assembling nanowires from gold NPs. Top right: assembling colloids into close-packed hexagonal arrays. Bottom left: Janus particle assembly. Bottom right: Assembling ellipsoidal particles.

Macroscopic viscous flows can be utilized to direct the assembly of nanoparticles into

ordered crystalline layers, which is another use of external direction to cause

nanoparticles to self-assemble. Viscous flow methods primarily make use of shear and

capillary forces to cause flow-induced ordering of nanoparticles on a substrate, which

generally produces large arrays of well-ordered and densely packed nanoparticles.[23]

The largest drawback of the viscous flow method is that controlling parameters such as

interparticle spacing and particle density is very difficult. Therefore, this method has a

limited amount of use when one desires to construct layered materials with finely tunable

optical and electronic parameters.

Directed SA refers to the manipulation of specific molecular interactions and

chemical compositions of nanoparticles to generate self-assembled structures. Ligand-

mediated self-assembly techniques have become especially attractive to those looking

to assemble complex layered materials, as they can provide fine levels of control over

the orientations of individual nanoparticles on a relatively large scale. A common method

for controlling assembly through ligand interactions is the chain length modulation of

attached surface ligands (Figure 2.5). Individual nanoparticles tend to exhibit strong van

der Waals attraction forces due to their size; these forces tend to maximize themselves

by creating interparticle contact points between the greatest available surface areas.[25]

Ligands placed on the particle surface can cause steric repulsion between nanoparticles;

this is a common technique used to prevent nanoparticle flocculation in solution.

However, the length of these ligands can be tuned to control the degree to which the

attractive van der Waals forces are able to pull nanoparticles together on a substrate.

Silver nanocubes, for example, will typically self-assemble into a "face-to-face"

configuration when short surface ligands are attached because the strong van der Waals

attraction between AgNCs exceeds the steric repulsive interactions between the surface

ligands.[28] When surface ligands are comparatively long, steric repulsion becomes

stronger than the weak van der Waals interaction, leading the self-assembly into an

"edge-to-edge" configuration.[28] The interplay between van der Waals attraction between

nanoparticles and steric repulsion between the attached surface ligands leads to

different equilibrium energies for the nanoparticle systems, which can be manipulated to

achieve controlled self-assembly on the scale of individual nanoparticles.
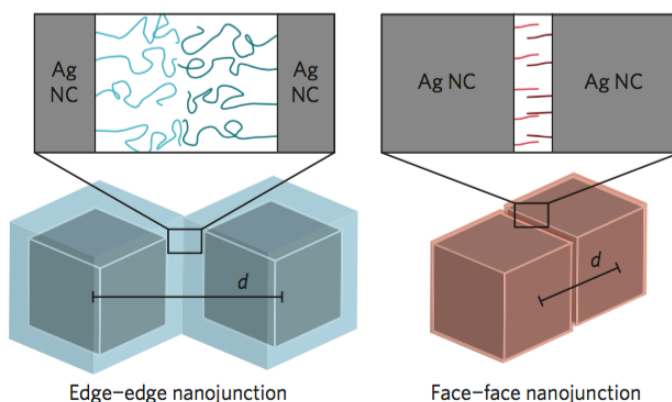
Figure 2.5 Diagram showing the different orientations into which AgNCs assemble due to varied surface ligand chain lengths. Systems with longer ligands adopt edge-edge configurations, whereas systems with shorter chains adopt face-face configurations.[28]

Functional group modification of the attached surface ligands also affects the

self-assembly scheme of NPs. Changing the functional groups at the end of the ligand

chain changes the "effective energy parameter" between the polymer chains and the

metal surfaces, ε_{PS}.[28] The value of ε_{PS} is generally determined by the binding affinity the

functional end group of the surface ligand possesses with the nanoparticle material.[28,29]

When ε_{PS} is small, the edge-to-edge configuration becomes more energetically favorable

with increasing ligand chain length, whereas a large ε_{PS} retains the face-to-face

configuration until much longer ligand chains are attached (Figure 2.6).[28]
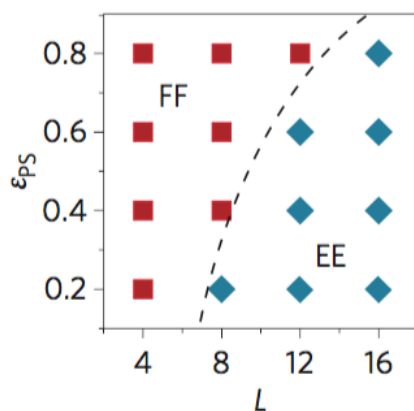
Figure 2.6 Graph showing the interplay between ligand chain length and ε_{PS} as it relates to nanoparticle assembly orientation.[28]
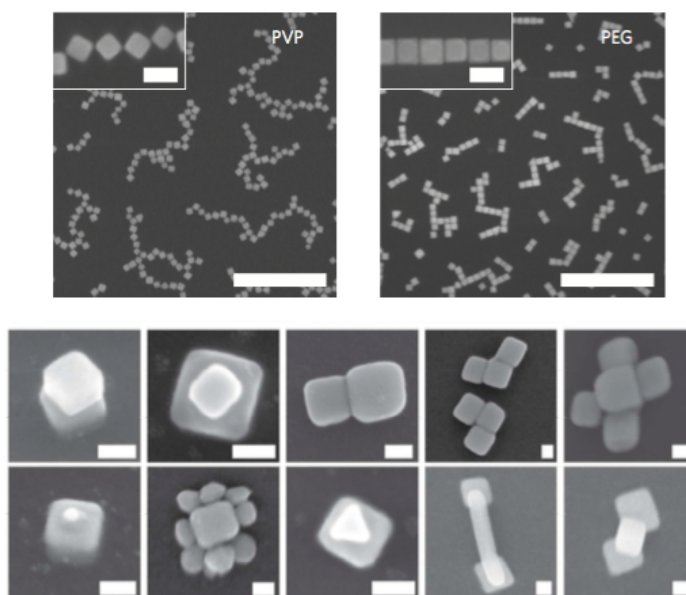
Figure 2.7 (Top) SEM images of assembled chains of AgNCs (scale bar = 1 µm, inset scale bar = 100 nm).[28] (Bottom) SEM images of self-assembled NP geometries achieved using precise control of surface ligand modifications and substrate embedding techniques (scale bars = 50 nm).[30]

The use of these chain length and functional group modulation techniques can be used

to fabricate a wide range of self-assembled nanoparticle "meta atom" geometries (Figure

2.7, above) with a high degree of accuracy, making them extremely valuable tools for the fabrication of functional layered materials. Although this method provides a great degree of control, perfecting the surface chemistry to achieve the desired structures is often very difficult. This leads to an inherent difficulty in making uniform nanoparticle layers across large (greater than 1 μm) size scales.
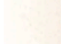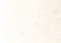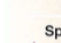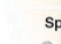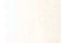
Self-assembly techniques that bridge the gap between externally directed assembly and directed self-assembly exist to offer precise arrangement of individual nanoparticles over comparatively large length scales. One such method is known as Langmuir-Blodgett (LB) assembly, which involves the deposition of a solution of nanoparticles suspended in a highly volatile solvent on an air-water interface in order to fabricate monolayer nanoparticle films (known as LB films). LB assembly frequently uses a tool known as an LB trough, a shallow Teflon dish accompanied by motorized Delrin plastic compression barriers, which is often used to control particle density. This Teflon dish is typically filled with water to form an interface on which to deposit a nanoparticle solution. Once a nanoparticle solution is suspended on the water surface, individual nanoparticles will become evenly dispersed across the surface in order minimize their interparticle repulsive interactions. Using the motorized compression barriers, the nanoparticle film suspended at the air-water interface can be compressed to achieve higher particle packing densities (which are typically controlled by monitoring the surface pressure of the air-water interface, Figure 2.8). Substrates can be immersed into this suspended film using dip-coating methods in order to transfer the nanoparticle array to a solid surface. LB assembly is one of the best methods for creating highly periodic nanoparticle arrays over large size scales with high repeatability, making it a highly desirable technique for making more complex layered materials. A more comprehensive discussion of LB assembly tunability will be seen later in Chapter 3.3.
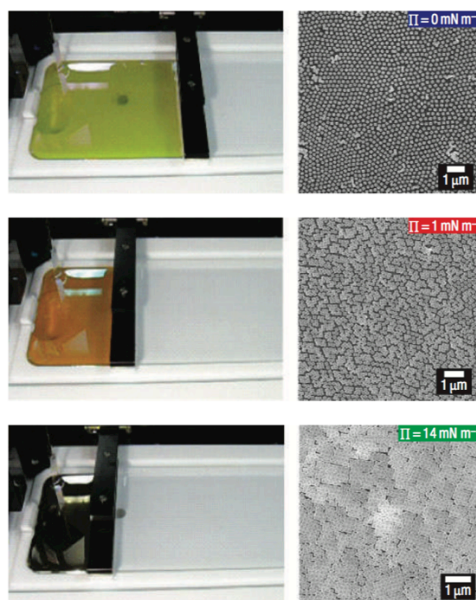
Figure 2.8 Pictures and accompanying SEM images showing the difference in LB film particle density for increasing surface pressure measured at the air-water interface.[8]

2.4 Methods for Assembling Layered Materials

As mentioned previously, layered materials are typically assembled using five distinct forms of "layer-by-layer" (LbL) deposition techniques, which include immersive, spin, spray, electromagnetic, and fluidic assembly techniques.[16] The adoption of these forms of LbL fabrication techniques over the past few years has signified a movement away from assembly techniques that rely solely on random diffusion-driven kinetics and towards the fabrication of more complex nanoscale systems and devices. Figure 2.9 shows a list of the most common techniques within each of the five major LbL fabrication forms, along with the fabrication parameters associated with each.

LbL ASSEMBLY TECHNOLOGY	BUILDING BLOCKS			PROCESS PROPERTIES		NANOFILM PROPERTIES		
	Substrates	Substrate sizes*	Layer materials	Time per layer	Automated (current status)	Layer thickness, nm†	Roughness, nm	Layer structure
Immersive		10 nm-1 m		10 s-12 h		<1-15	1-20	Interpenetrated
Dipping (2, 25)	Planar	1-100 mm	Polymers, colloids	10-30 s (32) or 10-20 min‡ (26)	Yes	1-2 (25, 26)	1-10 (44, 49)	
Dewetting (8)	Planar	1-10 mm	Polymers, colloids§	30-60 s (8)	No	1-2 (8)	NR	
Roll-to-roll (9)	Flexible planar	100 mm-1 m	Polymers	2-5 min (9, 34)	Yes	1-15 (9, 34)	15-20 (9, 34)	
Centrifugation (5, 6)	Particulate	10 nm-10 μm	Polymers, colloids	20+ min‖ (5, 6)	No	1-2 (5, 10)	3-10 (23, 94)	
Calculated saturation (12, 37)	Particulate	100 nm-1 μm	Charged polymers	5-10 min (39)	No	1-2 (39)	NR	
Immersive immobilization (33)	Particulate	100 nm-1 μm	Polymers	40-50 min (33)	Yes	<1 (33)	NR	
Creaming (11)	Emulsion	10 nm-1 μm	Polymers, colloids	0.5-12 h (11, 36)	No	1-7 (36, 38)	NR	
Spin		1-100 mm		10 s-5 min		<1-2	1-10	Stratified
Spin (14, 42, 43)	Planar	1-100 mm	Polymers, colloids	10-60 s (43)	Yes	<1-2 (42)	1-10 (44, 46)	
High gravity (15)	Planar	1-10 mm	Polymers, colloids	20 s-5 min (15, 49)	No	NR	1-2 (49)	
Spray		10 nm-10 m		<1 s-24 h		<1-15	1-10	Stratified
Spray (16, 52)	Planar	1 mm-10 m	Polymers	<1-30 s (59)	Yes	<1-5 (16, 51)	1-10 (51)	
Atomization (17)	None	10-100 nm	Charged polymers	12-24 h (17)	No	5-15 (17)	NR	
Spray immobilization (63)	Particulate	10-100 nm	Polymers	5-10 s (63)	Yes	2-4 (63)	NR	
Electromagnetic		10 nm-100 mm		1 s-20 min		1-20,000	10-30	Stratified
Electrodeposition (18, 20, 67, 73)	Planar	1-100 mm	Polymers, colloids	1 s-20 min¶ (65, 71)	No	2-20,000¶ (20, 67, 71)	10-30 (66, 70)	
Magnetic (19, 76)	Planar and Particulate	10 nm-100 mm	Polymers, colloids	15-20 min (19, 76)	No	1-2 (19, 75)	NR	
Electro-immobilization (13)	Particulate	10 nm-1 μm	Charged polymers	15-20 min (13)	No	2-3 (13)	NR	
Fluidic		100 nm-100 mm		10 s-45 min		<1-3	1-11	NR
Microfluidic planar (22)	Planar	10 μm-100 mm	Polymers	1-15 min (80, 81)	Yes	<1-3 (83, 84)	1-10 (80, 84)	
Microfluidic particulate (96-98)	Particulate	100 nm-10 μm	Polymers	10-60 s (96-98)	Yes	1-3 (96, 97)	NR	
Fluidized bed (23)	Particulate	1-10 μm	Polymers	3-5 min (23)	No	2-3 (23)	9-11 (23)	
Fluidic immobilization (86, 87)	Particulate	100 nm-1 μm	Polymers, colloids	5-45 min (86, 87)	No	1-2 (87)	NR	
Vacuum/filtration (21)	Particulate and fragile**	100 nm-1 μm	Polymers	10-20 min (95)	Yes	1-2 (94)	5-10 (94)	

Figure 2.9 A table showing common fabrication techniques involved in each of the five major LbL fabrication forms, as well as their typical usage and results parameters.[16] Reference numbers correspond to those from reference 16, not from this work.

Each of the five major LbL fabrication forms possesses distinct benefits when concerning the type of finished structure that is desired. Immersive assembly is by far the most common form of LbL assembly chosen, and is often chosen due to the great variety of choices concerning material and templates. Immersive methods typically involve the manual immersion of a planar substrate (either partially or completely) into a solution or interface containing the desired deposition material. Washing and rinsing steps are sometimes performed after immersion to remove any excess unbound material

from the surface. Immersive methods are very popular for creating layered materials, as

the immersion steps can be performed multiple times on a single substrate to create

multiple distinct layers; the thickness of the layers is determined by the thickness of the

particles being used. As an added benefit, substrates of any size or shape can be

uniformly coated with almost any type of particle using this method. The drawbacks of

immersive assembly methods are that they require relatively large amounts of

completion time, as well as large amounts of immersion material (much of which tends to

go to waste). Despite these downsides, immersive assembly continues to remain the

industry standard of LbL fabrication, and is used to create devices such as LEDs,[31]

flame-retardant coatings,[32] antireflective/antifogging coatings,[33] and much more.

Spin assembly is another very common method of LbL assembly, involving

casting a particle solution onto a spinning substrate, or onto a stationary substrate that is

then spun.[16] Particle solutions that are spun at high speeds on a flat substrate

experience strong electrostatic, shear, and viscous forces that pull particles across the

substrate surface, causing them to assemble into very homogenous layers. Compared to

immersive assembly, spin assembly can be completed much more quickly and can be

used to generate layers of widely varying thicknesses that correspond to spin speed.

Although spin assembly typically results in much more uniform and complete particle

monolayers than immersive assembly (Figure 2.10), spin assembly techniques are

greatly limited by the fact that only small planar substrates can be used effectively.

Depositing multilayer films also becomes difficult with successive depositions due to the

shear forces involved in spinning stacked layers.[16]
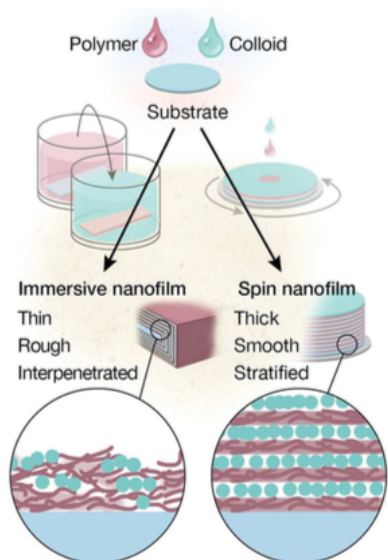
Figure 2.10 Difference between the quality of successive particle monolayers between purely immersive assembly and spin assembly.[16]

Spray assembly makes use of aerosolized particle solutions to deposit layers of films onto substrates. The resultant film characteristics are highly tunable using spray assembly, as spraying parameters such as suspension concentration, spray flow rate, spray duration, resting duration, and post-spray washing all have an effect on surface morphology an uniformity.[16] Much like spin assembly, spray assembly films possess more distinct layers than those of immersive assembly. The main advantages of spray assembly are that the potential for automation is very high and that very large substrates can be evenly coated very quickly. However, spray assembly techniques are somewhat limited by the effects of gravity draining as well as limitations imposed by spray nozzle equipment.[16]

Electromagnetic assembly techniques (such as the externally directed self-assembly examples mentioned in section 2.3) rely on the application of an electric or

magnetic field to form particle layers. Electromagnetic assembly is similar in principle to immersive assembly, in that substrates are often immersed in a solution containing the particle to be deposited. However, electromagnetic assembly differs in that the use of electric or magnetic fields allows for the controlled assembly of particles that are chemically or mechanically sensitive. It is also much faster than immersive assembly, and yields much denser particle films with thicknesses that are directly controllable via the modulation of the applied field strength. The use of electromagnetic assembly to form LbL materials is not as common as the other methods, as it often requires specialized equipment and is ultimately not as versatile.[16]

The last major LbL fabrication form is fluidic assembly, which involves flowing a particle solution through a fluidic channel that contains a fixed substrate. The main benefit of fluidic assembly over the other four methods is that it is well suited to substrates of three-dimensional complex geometries, such as hollow tubes and cage-like structures.[16] Region-specific patterning is also possible by using "masking" techniques to prevent particle adhesion to selected parts of the substrate. The potential for automation and large-scale manufacturing is possible with fluidic assembly techniques, but they are often disadvantaged by the need for special equipment and complicated setup procedures.[16]

Out of the five major forms of LbL assembly techniques, immersive assembly will be the most relevant for the experiments conducted throughout the rest of this work. Specifically, the use of the Langmuir-Blodgett technique will be the primary method for fabricating layered nanoparticle materials in order to form what are known as "metamaterial" structures.

2.5 Why Layered Materials?

Layer-by-layer assembly provides a degree of simplicity, versatility, and nanoscale control that other fabrication methods simply do not. These qualities make LbL assembly one of the most widely used technologies for coating both planar and particulate substrates in a diverse range of fields, including optics, energy, catalysis, filtration, semiconductors, and biomedicine.[16] An area of study in which layered nanoparticle materials have become very important is the field of metasurfaces (MSs), which are ultra-thin arrays of sub-wavelength resonators that exhibit optical properties not found in any natural material.
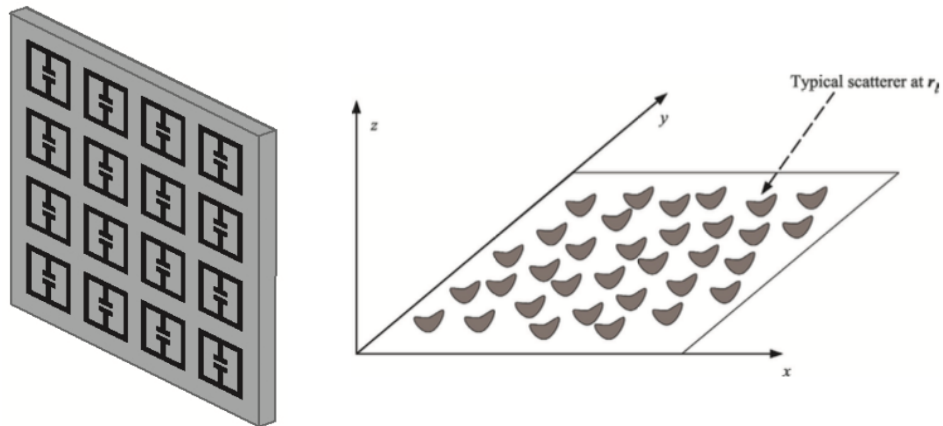
Figure 2.11 Metasurfaces constructed using a repeating array of a type of split-ring perfect scatterer (left) and an arbitrarily shaped scatterer (right).[36]

Some of the most extensive research into optical metamaterials and metasurfaces (the two-dimensional analog of metamaterials) since the early 2000s has been conducted by David Smith and his research associates.[34] A majority of this work has focused on using nanostructured surfaces in order to produce materials with unique optical properties, such as negative refractive indices, artificial magnetism, negative resonant response, sub-wavelength resolution, and perfect light absorption.[34, 35] Some of

the patterned surfaces Smith has examined have complicated geometries resembling split-ring resonators designed to perfectly scatter incident light, whereas some of the surfaces have more arbitrary shapes that somewhat resemble nanoparticles (Figure 2.11, above).[36] The practical result of these structures are thin film surfaces that exhibit near-perfect absorbance at specific "resonant" wavelengths (Figure 2.12).
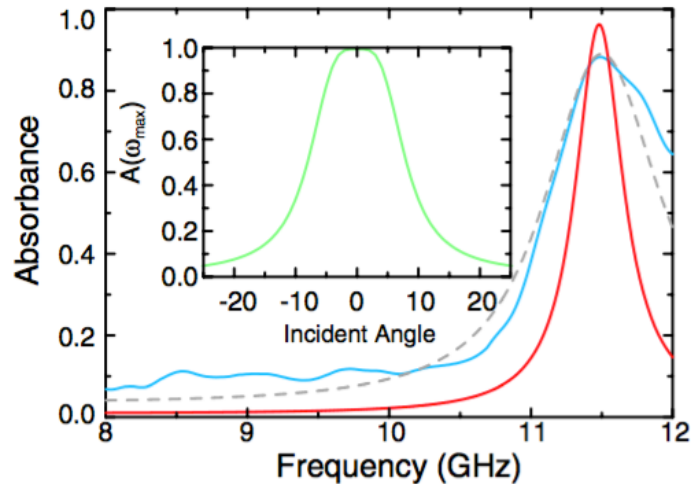
Figure 2.12 Main panel shows the simulated (red) vs. measured (blue) absorbance of the split ring structure under white light. The green inset shows simulated angular dependence.[35]

David Smith and his associates have also demonstrated that fabricating a metasurface is possible by utilizing colloidally synthesized metal nanoparticles such as silver nanocubes.[43] In this work, AgNCs were more or less randomly deposited onto a layered substrate consisting of a plasmonic gold film and a dielectric spacer layer via solution exposure. A LbL deposition of polyallylamine hydrochloride and polystyrene sulfonate was used to control the height of the dielectric spacer layer and the interparticle spacing of the AgNCs was controlled by varying the concentration of the AgNC solution in which the substrates were immersed. The results of these experiments were metasurface structures that possessed similar optical properties to Smith's top-

down structures, yet had increased flexibility due to the nature of their construction techniques (Figure 2.13). However, the interparticle spacing control in Smith's experiments was somewhat limited by the random diffusion-driven AgNC assembly techniques, which led to MSs with somewhat random and unordered surface morphologies (Figure 2.13). This random ordering often had adverse effects on the MS optical properties, as well as on the prospects for controlled assembly over a relatively large area. The use of LbL assembly to controllably fabricate large-area well-ordered MS structures using colloidal metal NPs has been the focus of other work,[3] and will be the primary method for device construction throughout this work as well.
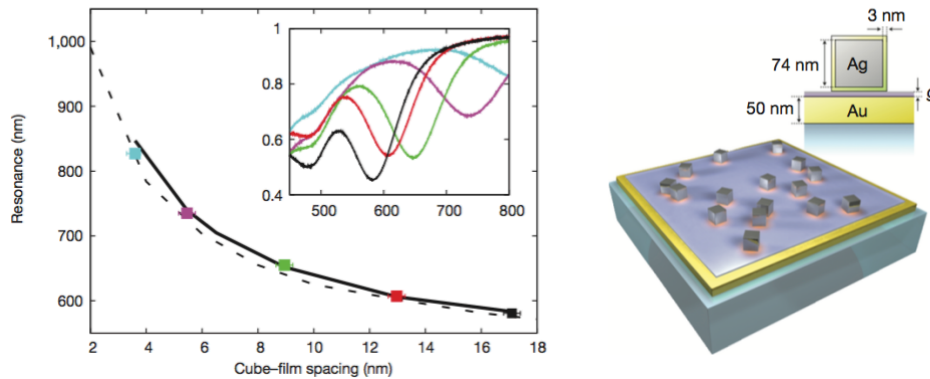
Figure 2.13 Curve showing the relationship between resonance wavelength and interparticle spacing of colloidal AgNC-based MSs by David Smith's group (left), as well as a diagram illustrating the unordered nature of the AgNC layer.[43]

Layer-by-layer assembly methods can be applied to construct similar types of metamaterials and metasurfaces using deposited layers of well-ordered colloidal nanoparticles, precious metals, and dielectrics.[3,7,8] The benefit of colloidal metasurfaces is that they are easily tunable to fit different optical profiles and have the potential to be fabricated on a larger scale much more easily than metasurfaces that require conventional top-down fabrication approaches. The fabrication and use of these well-

ordered colloidal metasurfaces to observe novel optical effects will be the focus of the

remainder of this work.

CHAPTER 3: COLLOIDAL METASURFACE CONSTRUCTION

3.1 Layered Metasurfaces

As mentioned previously, metasurface structures can be fabricated using bottom-up layer-by-layer assembly methods by depositing specifically selected layers of noble metals, dielectric spacer materials, and colloidal metal nanocrystals.[3,7,8] What makes bottom-up surfaces fabricated using colloidal nanoparticles better than their top-down counterparts is their ability to be modified to exhibit optical properties such as near-perfect absorbance at a range of wavelengths.[3] By controlling factors such as particle size, particle packing density, substrate material/thickness, and dielectric layer thickness, the resonant wavelength of the surface can be shifted throughout the visible and near-infrared (NIR) light spectrum to any wavelength that is desired. Additionally, the LbL assembly technique allows for the incorporation of active layers into the plasmonic gap without affecting the integrity or morphology of the active layer material. This section will focus on the fabrication of a colloidal metasurface structure with an incorporated active layer of semiconducting cadmium selenide QDs (Figure 3.1) in order to observe the effects that plasmonic gap resonance has on the absorptive and emissive properties of the QDs.
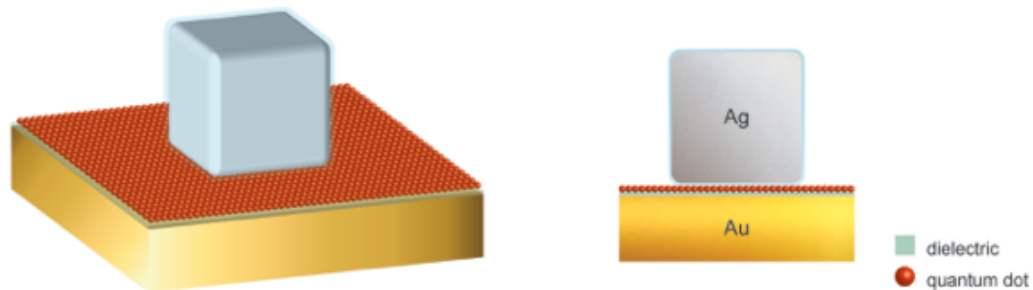
Figure 3.1 A schematic roughly showing the general colloidal MS structure with a quantum dot active layer placed within the MS resonance cavity (between the Au layer and the AgNC).

3.2 Colloidal Metasurface Construction Materials

3.2.1 Silver Nanocubes

The materials chosen to construct the metasurface were chosen due to specific qualities that affect the properties of the fabricated surfaces. Silver nanocubes (AgNCs) were chosen for the metal nanocrystal layer for several reasons. One such reason is because silver has a plasmonic response frequency that reaches into the visible spectrum. Silver also produces a much stronger plasmonic response than and is much cheaper than gold, the second most common plasmonic particle material. Silver NPs can also be synthesized in a variety of polyhedral and non-polyhedral geometric shapes (both single and multi-crystalline), such as platelets, spheres, cubes, prisms, rods, wires, and octahedra,[6] that each produces a unique surface plasmon patterns. The reason the cube geometry was chosen is because the flat faces of a cube possess a larger contact area per volume than any of the other particle geometries. This large contact area leads to a very strong LSPR effect, and therefore enhanced electromagnetic field, in the region between the cubes and their underlying substrate. The combination of all of these qualities exhibited by the silver nanocube leads to a nanoparticle with a very strong visible-range plasmonic response that exhibits high degrees of both in-plane and out-of-plane coupling and that is fairly simple to synthesize and incorporate into a layered structure.

The silver nanocubes used throughout these experiments were synthesized via a polyol reaction[6,37] using silver nitrate, pentanediol, copper chloride, and a capping agent of polyvinylpyrrolidone (PVP). The silver nitrate serves as a precursor for the growth of crystalline silver seed precursor particles, and the pentanediol serves as both the diffusion-limiting viscous solvent and reducing agent. The copper chloride is introduced to ensure a homogenous nucleation of single-crystalline seeds, which are crucial to the

formation of monodispersed AgNC solutions. The silver seeds (Figure 3.2A) are first

formed by a long sonication of silver nitrate salt in pentanediol in the presence of copper

chloride. The copper chloride is bifunctional in the reaction: it reacts with present oxygen

to form an oxidative etchant to etch multiply and/or singly twinned crystal seeds into

single-crystalline seeds necessary for cube formation, as well as helping to prevent the

fast reduction of metal ions that leads to twinned particles via the formation of silver

chloride (which is insoluble at low temperatures). Once prepared, the seed solution is

then rapidly injected in small amounts into a flask of pentanediol at approximately 195 °C

every minute. Small amounts of PVP/pentanediol solution are injected into the same

heated solution every 30 seconds. Upon heating, the pentanediol oxidizes to form an

intermediate $HO(CH_2)_4COH^{2+}$; the silver nitrate salt is then reduced to form crystalline

silver, with byproducts of nitric acid, water, and acetylacetone. Typical byproducts that

are also seen are glutaraldehyde and 1-hydroxypentanoic acid, which result from the

overheating and self-reduction of the pentanediol solvent. The PVP selectively interacts

with the various crystal facets of FCC silver through weak physisorption, suppressing

crystal growth rate of the (100) planes and effectively limiting growth to only the (111)

planes. The PVP also acts as a capping agent to prevent oxidation or degradation of the

synthesized cubes. Following synthesis, the AgNC solution is subjected to vacuum

filtration to decrease polydispersity and remove non-cubic particle byproducts.

Synthesized solutions of nanocubes typically exhibit unique colors due to their

plasmonic interactions with light (Figure 3.2B) and are often monodisperse in size

(Figure 19C). UV-Vis spectra display unique features that correspond to the plasmonic

modes associated with the particle geometry (Figure 3.2D). The large dipolar peak

represents plasmonic oscillation across cube faces, whereas the smaller peaks

correspond to oscillations between corners and other features.
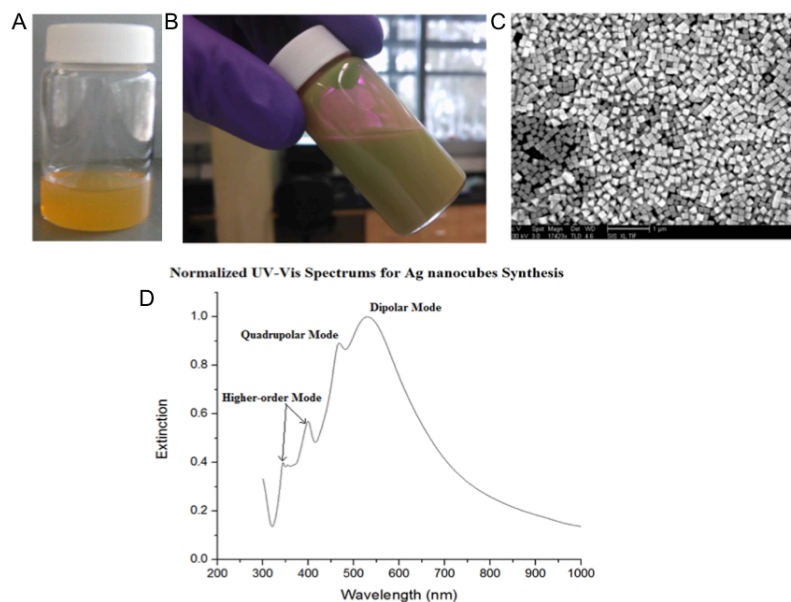
Figure 3.2 Various figures associated with AgNC synthesis, including a photo of the silver seed (A) and finished cube (B) solutions, an SEM image of filtered AgNCs (C), and a simulated AgNC solution spectrum (D).

3.2.2 Cadmium Selenide Quantum Dots

      The material chosen to form the active layer was CdSe quantum dots. Quantum dots are fluorescent semiconducting nanoparticles that exhibit tunable fluorescent wavelengths based on their size. They typically range from approximately 2 to 10 nm in diameter and contain between one hundred to a few thousand atoms.[38] Their existence within this size range allows them to retain properties possessed by bulk CdSe, but renders them susceptible to quantum mechanical effects. In bulk semiconductors, electronic bandgap is dictated by the location of electronic energy states within a material, which in turn is dictated by the composition of the material itself. In semiconducting quantum dots, the size of this bandgap is also affected by the quantum dot size, which causes quantum dots to exhibit tunable emission wavelengths that

typically span from about 400 nm to 750 nm. Larger QDs tend to emit at longer

wavelengths, since they are more similar in electronic structure to the bulk material,

whereas smaller QDs emit a shorter wavelengths (Figure 3.3) due to the effects of

quantum confinement. By manipulating QD size and material composition, a wide range

of possible emission schemes can be synthesized to fit experiment requirements. A

more comprehensive explanation of QD electronic properties will be given during

Chapter 4.

Figure 3.3 Pictures demonstrating the tunability of QD emission color with regards to size under normal light (left) and UV light (right). As QD size increases from left to right, emission wavelengths are 490 nm, 530 nm, and 580 nm.

The CdSe quantum dots used throughout these experiments were obtained from

two separate sources. For the two-photon enhancement experiments (Chapter 5),

CdS_xSe_{1-x}/ZnS core/shell quantum dots were purchased from Sigma Aldrich as 1 mg/mL

colloidal solutions in toluene (Figure 3.3, above). For the single-photon enhancement

experiments (Chapter 4), CdSe/ZnS core/shell quantum dots were synthesized via a

high-temperature pyrolysis method according to procedures published elsewhere.[38]

First, a selenium precursor is made by dissolving pure Se powder in a 1-Octadecene

and Trioctylphosphine solution at 150 °C in a nitrogen atmosphere. A second solution

containing CdO powder, 1-Octadecene, and Oleic acid is then placed into a flask and purged with nitrogen, followed by heating up to 260 °C. Once the cadmium precursor solution reaches stable temperature, the selenium precursor is rapidly injected and the reaction is allowed to proceed until the desired QD size is achieved. To add ZnS shells to the QDs (which improve chemical/photostability and increase quantum yield),[38,39] a small aliquot of the CdSe QD solution is placed into another flask and heated to 160 °C. A solution of Tributylphosphine and Hexamethyldisilathiane is added dropwise to the heated QD solution over the span of a few minutes. After a minute of reaction time, the final CdSe/ZnS core/sell QD solution is removed from heat and washed several times with anhydrous methanol to remove any organic byproducts or unreacted precursor.

Synthesized and purchased quantum dots often have noticeably colored solutions at high particle concentrations (Figure 3.3, above), but can also appear optically clear at lower concentrations due to the very small absorption cross section of the QD particles. The synthesized CdSe/ZnS QDs were typically between 4 nm and 6 nm in diameter and exhibited very sharp absorbance peaks (Figure 3.4). The narrowness of the absorbance profile was a highly desired feature for the QD active layer within these experiments, the reason for which will be explained in Chapter 4.
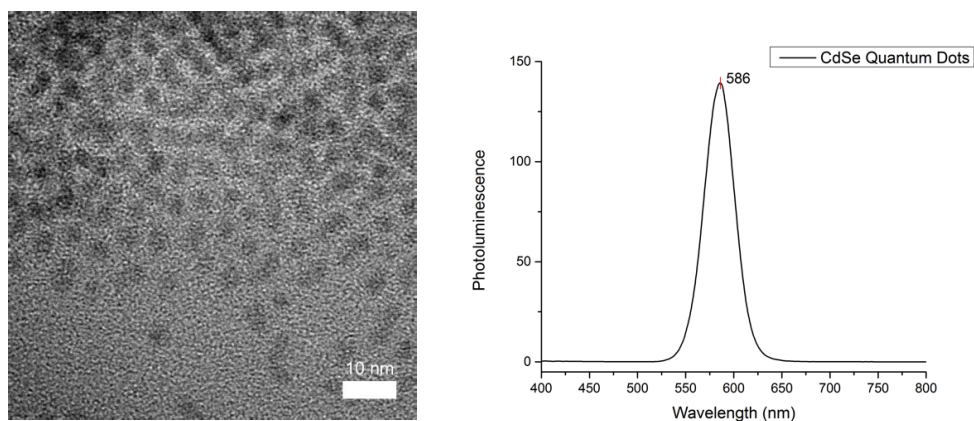
Figure 3.4 TEM image of synthesized CdSe QDs (left) and fluorescence spectrum of synthesized CdSe QDs (right).

3.2.3 Substrate Materials

The materials chosen to form the substrate were often chosen for much more simple reasons than the active and particle layers. The main backing was chosen to be soda-lime glass, as it provided a relatively smooth surface on which to fabricate successive layers. These large wafers were then cut into 10 mm^2 squares using a dicing saw. Once sized, the individual wafer squares were cleaned with piranha solution, a 3:1 mixture of concentrated sulfuric acid and 30% hydrogen peroxide, to remove any organic or inorganic contaminants. To create the bottom half of the plasmonic junction necessary for enhancement, a layer of gold was placed on the substrate. Gold has similar plasmonic properties to silver, but tends to exhibit resonance strengths much less than those of silver. However, gold is much more inert than silver and as such requires no surface modification to prevent the occurrence of oxidation that could lead to poor plasmonic response. Additionally, gold forms atomically smooth layers much more easily than silver, which is essential to creating a uniform surface with uniform optical properties. The piranha-cleaned substrates were placed into a high vacuum sputter chamber (specifically, a Denton Discovery 18 Sputterer system), and cleaned for 60 seconds with a 100 Watt RF argon plasma to remove any contamination that may have resulted during substrate transfer between the working lab and the sputter system. The substrates were then sputtered with an approximately 15 nm chromium adhesion layer, followed by an optically thick (80 nm) gold layer. Pure 10 mm^2 silicon substrates were also used to fabricate some of the control samples.

Dielectric spacer layers were created using a few different methods. Dielectric layers between 0.1 – 2 nm were fabricated by employing the formation of self-assembled monolayers (SAMs) of alkanethiols on the sputtered gold surface. An example of one alkanethiol ligand used to form SAMs was 1-Hexadecanethiol (1-HDT), which typically

formed SAMs approximately 1 nm in thickness. Piranha cleaned gold substrates were incubated in 1.0 mM ethanolic alkanethiol solutions for approximately 18 hours until SAMs formed, and were then sonicated briefly to remove excess physisorbed molecules. The pure silicon substrates were sometimes coated with a layer of Hexamethyldisilazane (HMDS), which acts as an adhesion layer to prevent film delamination during the LB dipping process.

3.3 Use of Langmuir-Blodgett Assembly Techniques

Langmuir-Blodgett assembly is a form of bottom-up dip-coating assembly, which is in turn part of the larger class of immersion assembly techniques. As mentioned previously, LB assembly involves the deposition of nanoparticles suspended in a highly volatile solvent (such as chloroform or toluene) on an air-water interface in order to form monolayer NP films on substrates of practically any geometry. LB films can be created at any simple air-water interface, such as the convex water surface of a filled petri dish, but are often created using a device known as an LB trough (Figure 3.5).
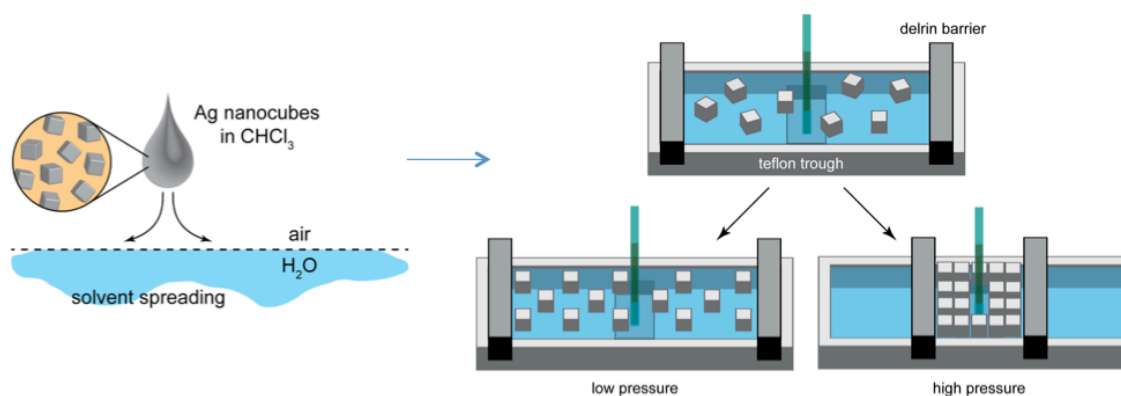
Figure 3.5 A diagram showing the deposition of an AgNC solution in chloroform onto the surface of a LB air-water interface via drop casting. The Delrin barriers of the LB trough can be compressed to achieve different particle densities.

As seen in Figure 3.5, an LB trough is a shallow Teflon plate with attached barriers made out of Delrin plastic. This trough is filled with water to form an interface on which to deposit a nanoparticle solution. Nanoparticles deposited onto this interface will naturally disperse into a monolayer film with an equilibrium packing density determined by the minimization of interparticle repulsive interactions. The motorized Delrin barriers can then be compressed to yield nanoparticle monolayers with an interparticle spacing tunable from several hundred nanometers to only a few nanometers (Figure 3.6). Dipping a substrate into this film will cause the film to transfer to the substrate surface.
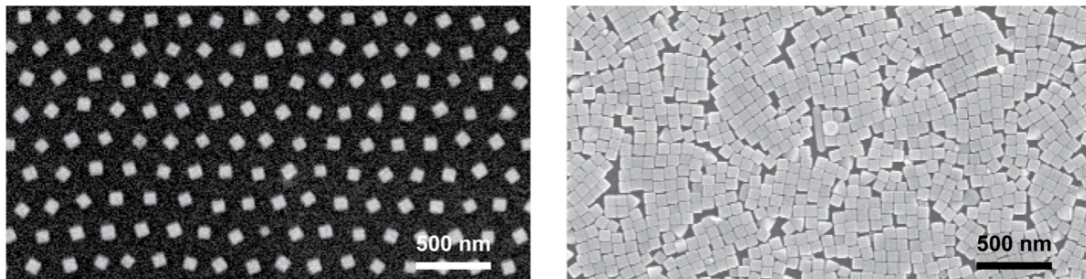
Figure 3.6 Examples of highly uniform AgNC films made using an LB trough dip-coating method. Films made at lower surface pressures (left) are less densely packed than those made at higher surface pressures (right).

LB assembly is a very useful technique for assembling nanoparticles, particularly for making colloidal metasurface structures, because of the degree of fine control is provides over the fabrication of large, uniform nanoparticle arrays with a high degree of repeatability and high throughput. However, when fabricating colloidal metasurfaces, we are also concerned about the ability to easily and repeatedly fabricate colloidal metasurfaces that display a range of different optical responses throughout the visible and NIR spectra.[3] The use of LB techniques to manipulate the particle density of NP films allows for the tuning of the MS structure fundamental resonant wavelength.[3] MS fundamental resonant wavelength (also known as the "fundamental mode") is partly

governed by the degree of in-plane interparticle coupling exhibited by the nanoparticle film, which is directly related to the interparticle spacing between adjacent nanoparticles. Increasing nanoparticle density results in a "quasi-continuous resonance" from the coupled LSPRs of adjacent NPs. The coupling of this quasi-continuous LSPR with the underlying gold film has the effect of broadening and redshifting the fundamental mode of the MS structure due to the effects of radiation damping.[3] By using LB assembly to finely control this interparticle spacing (via a control of surface pressure during the assembly process), the resonant wavelength of the colloidal MS can be precisely tuned to a desired value (Figure 3.7).
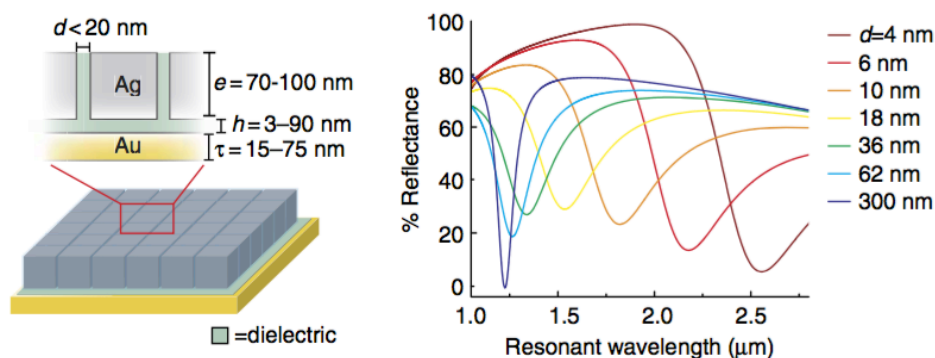
Figure 3.7 Simulation showing the tunability of colloidal MS fundamental mode by manipulating interparticle spacing via LB assembly. Fundamental mode redshifts as interparticle spacing decreases.[3]

For these particular experiments, the QD layers were deposited onto the sputtered gold/dielectric surface by high-speed spin coating in toluene. Only low-density AgNC films were required to complete the MS structure, and thus the use of a petri dish LB film was sufficient to achieve a the MS resonance frequencies desired for the QD emission enhancement experiments. After vacuum filtration, an AgNC sample was concentrated and washed in excess ethanol several times using a centrifuge. The final

washed solution was dispersed in chloroform and then deposited dropwise onto a
deionized water subphase created in a small petri dish. The nanocube film formed at the
air-water interface (Figure 3.8) was allowed to disperse for 30 minutes to ensure the
formation of a uniform film with low-density packing. The AgNC film was then transferred
onto QD-coated substrates by dipping them into the subphase by hand with an
orientation parallel to the film surface.
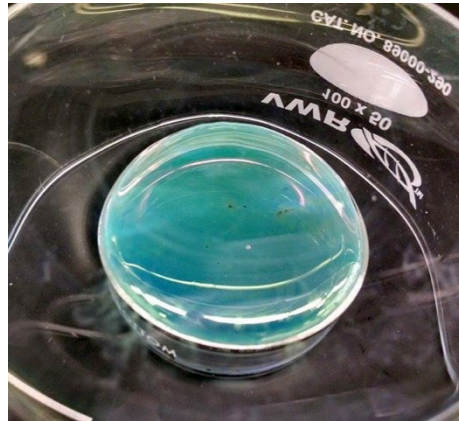
Figure 3.8 A photo of an AgNC LB film made using a small glass petri dish. The convexity of the
water surface creates a similar surface generated by an LB trough.

3.4 Additional Metasurface Tunability

Since electromagnetic coupling increases exponentially with decreasing
distance, the degree of coupling between AgNCs (which is controlled by particle packing
density) is the primary determinant of the MS fundamental resonance frequency.[3]
However, there are also a few other ways to control the MS fundamental resonance
wavelength by changing the fabrication parameters. Altering the size of the
nanoparticles is one such way. For AgNCs, the wavelength of the fundamental mode
increases linearly with nanocube size (Figure 3.9).[3] This is due to the linear increase in
dipolar resonance wavelength for non-coupling colloidal nanocubes of increasing size,

as well as a decrease in absorption efficiency of the fundamental mode that stems from the increased scattering cross-section of larger particles.[3,40] Dielectric spacer height also affects the wavelength of the fundamental mode, as increased dielectric spacer height leads to weaker out-of-plane electric field confinement between the AgNCs and the gold substrate and increases in-plane coupling between adjacent AgNCs (Figure 3.9).[3] Thus, increased dielectric spacer height redshifts the fundamental mode wavelength of the metasurface. The thickness of the gold substrate layer also affects the fundamental mode wavelength to a certain degree, as a thicker gold layer leads to a blueshift in the fundamental mode wavelength. However, this parameter has the least effect on the fundamental mode position than the other fabrication parameters.
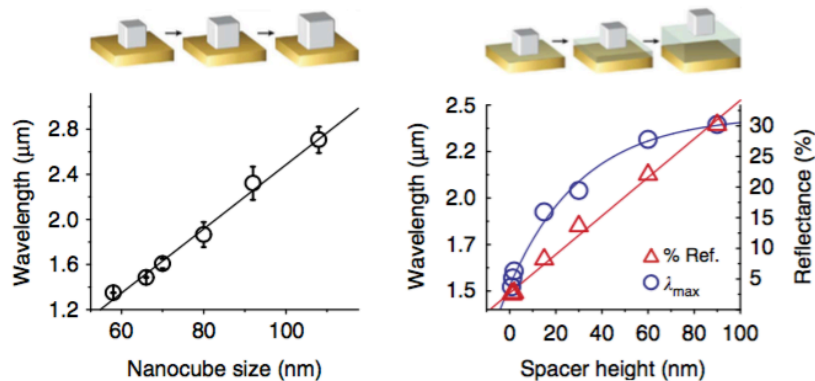
Figure 3.9 Curves demonstrating the relationship between MS fundamental mode resonance wavelength, AgNC size (left), and dielectric spacer height (right).[3]

The result of fabricating these metasurface structures is the creation of a layered nanoscale surface with a total thickness on the order of about 100 nm that displays optical properties that are different from the sum of its individual components and ultimately not seen in nature (Figure 3.10). The intensely localized electromagnetic field created in the resonance gap can in turn be used to enhance the properties of any active

layer material that resides within it. Although many of the figures in this section that

detail the tunability of the metasurface (specifically 3.7 and 3.9) show that the

metasurface fundamental resonance wavelength resides within the NIR range, it is

possible to tune these metasurfaces to exhibit resonance modes within the visible range,

which will be taken advantage of in the following QD emission enhancement

experiments in Chapter 4 and 5.
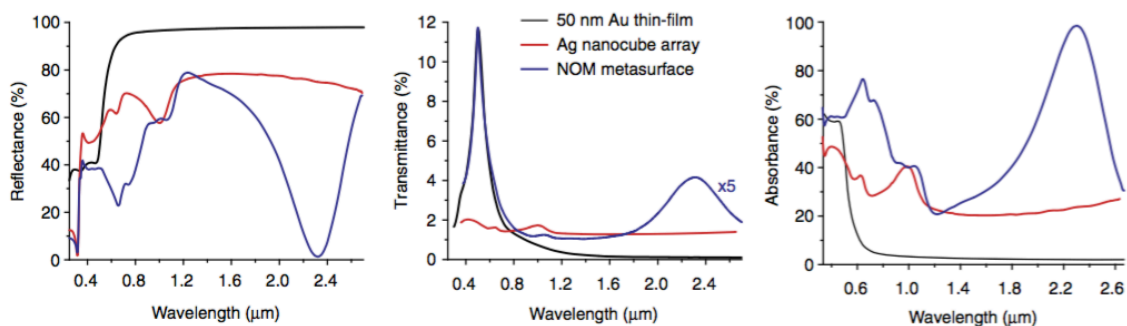
Figure 3.10 Curves demonstrating the reflectance, transmittance, and absorbance properties of a nanocube-on-metal (NOM) metasurface structure compared to the properties of its constituent components.[3]

Overall, colloidal metasurface structures possess a wide range of flexibility as

they can be fabricated using different types of substrates, different nanoparticle

shapes/sizes, different metals, and other parameters alongside those already discussed.

The great potential for their incorporation into larger functional structures is largely due

to this customizability.

Chapter 3 in part is currently being prepared for submission for publication of the

material. Rozin, Matthew J,; Brown, Eric R.; Tao, Andrea R. The thesis author was one

of the primary investigators and authors of this material.

CHAPTER 4: SINGLE-PHOTON ENHANCEMENT

4.1 Basics of Quantum Dots

As mentioned previously, quantum dots are fluorescent semiconducting

nanoparticles that exhibit tunable fluorescent wavelengths based on their physical size,

which typically ranges between 2 to 10 nm in diameter. This size range places them in a

unique class of materials that possess some of the properties of the bulk material, yet

are susceptible to quantum mechanical behavior. This quantum mechanical behavior,

known as "quantum confinement," is what is responsible for the tunable nature of

quantum dot fluorescent wavelengths. Before the concept of quantum confinement can

be discussed, a few basic concepts about semiconductor materials must be discussed

first.

Semiconductors are a class of solid-state materials that are typically defined by

the relative positions of their electronic valence and conduction bands. In conducting

materials such as copper and other metals, the highest occupied and lowest unoccupied

electron states are not separated by an energy gap (or "bandgap", E_g) that is common to

semiconductor and insulator materials. This bandgap acts as an energy barrier across

which electrons in the valence band must travel to reach the conduction band. In

insulators, bandgaps are typically so large that electrons are effectively prevented from

transitioning to the conduction band, which makes insulators nonconductive.

Semiconductors have bandgaps in between those of conductors and insulators, which

range between 1 – 4 eV. Under certain conditions, electrons can traverse bandgaps of

these sizes, which allows semiconductors to behave either like conductors or insulators

in given circumstances. Figure 4.1 demonstrates the relative bandgap sizes between

different types of materials: for conductors E_g < 0.1 eV, for semiconductors E_g = 0.1 –

3.5 eV, and for insulators E_g > 3.5 eV.[38]
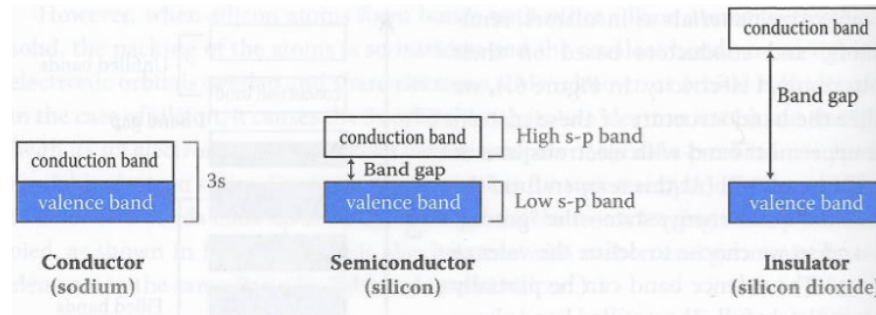
Figure 4.1 Illustration depicting the relative bandgap sizes of conductors, semiconductors, and insulators.[41]

In fluorescent semiconducting materials such as quantum dots, the size of this electron bandgap determines the electron-hole recombination distance and therefore the wavelength of absorbed and emitted photons. It is the effect of quantum confinement that changes the bandgap sizes of nanoscale semiconductor particles from that of their respective bulk semiconductor. To understand quantum confinement, we must examine the way that electronic states behave in atoms, molecules, and then finally in bulk solids. In individual atoms, electrons reside at degenerate, discrete energy levels according to the solutions of the Schrödinger equation (Equation 1).

$$E_n = \frac{3\hbar^2 n^2}{2m^* a^2}$$

Equation 4.1 Discretized energy levels of electrons according to Schrödinger's equation.

When atoms are brought closer together to form molecules, the electron clouds of each individual atom begin to interact and the degenerate states split into different energy levels.[38] If we continue to add atoms to the point where the material is now bulk, these energy levels have split so many times that they have effectively blended together into electron "bands" because the energy differences between individual levels have become

so small that the differences are practically negligible. This discretization of energy levels

that occurs in atomic structures is illustrated in Figure 4.2.
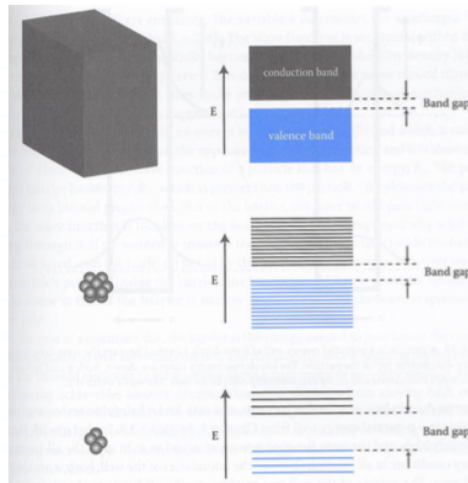
Figure 4.2 Illustration depicting the formation of energy bands as small groups of atoms/molecules approach bulk dimensions.[41]

The discretization of energy levels that occurs as bulk structures begin to approach

molecular dimensions is due to the confinement of electron-hole pairs (or "excitons") to

spaces smaller than that of the Bohr exciton radius, or the spatial separation between

the electron and the hole that is left behind when the electron crosses the bandgap.[38] As

excitons become confined to a dimension, less energy states at which an electron can

exist are available. Confinement to all three dimensions causes states to become more

or less discrete, similar to the discrete states of a single atom (Figure 4.3).
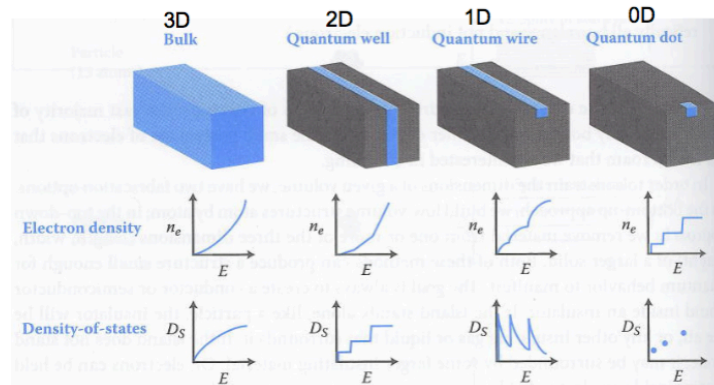
Figure 4.3 Discretization of available electron states as material dimensions become confined below the Bohr exciton radius in all three dimensions.[41]

A quantitative expression for the effect of electronic state discretization on material bandgap can be seen in Equation 2. By manipulating the physical size of QDs, their fluorescent properties can be manipulated as well. The manipulation of their fluorescent properties is crucial in order to achieve enhanced emission via their integration into a colloidal metasurface.

$$E_g \ = \ E_{g\,(bulk)} + \frac{\hbar^2 \pi^2}{2a^2}\left[\frac{1}{m_e^*} + \frac{1}{m_h^*}\right] - \left(\frac{1.8e^2}{4\pi \varepsilon_m a}\right)$$

Equation 4.2 The quantitative calculation of quantum dot bandgap from bulk bandgap with respect to material dimensions.[41]

4.2 Why is Single-Photon Enhancement Desirable?

The concept of "quantum yield" is often used when describing various fluorescent entities. The quantum yield (QY) of any radiation-induced process is generally defined as the number of times that a specific event occurs per absorption of a photon in the system. For fluorescent particles such as fluorophores or quantum dots, QY is expressed generally as the ratio of photons emitted to photons absorbed (Equation 4.3).

$$\Phi = \frac{\# \ Photons \ Emitted}{\# \ Photons \ Absorbed}$$

Equation 4.3 General QY of any fluorophore or fluorescent particle.[42]

Quantum yield is typically measured by measuring the yield of a particle relative to that of a fluorophore of known QY under the same experimental parameters.[42] This calculation for QY is quantified by Equation 4.4.

$$\Phi = \ \Phi_R \times \frac{Int}{Int_R} \frac{1 - 10^{-A_R}}{1 - 10^{-A}} \frac{n^2}{n_R^2}$$

Equation 4.4 QY calculated relatively by using the known QY of another fluorophore.[42]

Quantum dots and many other fluorescent particles are often rated by their fluorescent quantum yields, or their apparent emission intensity per particle, as well as other characteristics like absorption/emission ranges and absorption cross-sections. Quantum yield is often an intrinsic property, but can at times be influenced by external environments. The colloidal MS used in these experiments is one such environment, as it dramatically enhances the quantum yield of the encapsulated QDs by exposing them to high-intensity local electric fields. Increased quantum yield using plasmonic metasurfaces has the potential to greatly improve the efficiency and usefulness of many forms of photonic devices, such as photovoltaics[43] and optical sensors[44,45].

4.3 Single-Photon Enhancement Mechanism

In order to understand the way that the colloidal metasurface enhances the emission of the QDs, we first must examine the way in which single-photon absorption and emission processes work in QDs and other fluorophores. When incoming photons possess a discrete energy greater than that of the material bandgap, the photon is

absorbed. This photon absorption excites an electron from an energy state in the

conduction band to an energy state in the conduction band, leaving behind a hole

(Figure 4.4).
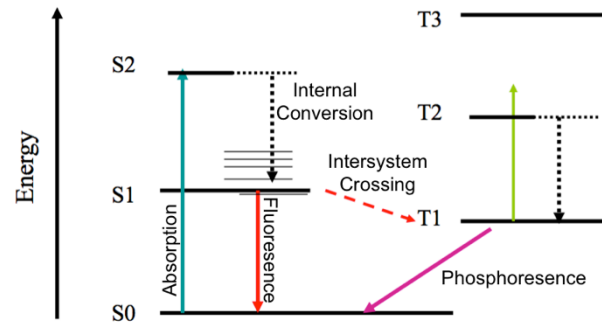
Figure 4.4 Diagram illustrating the concept of photon absorption/emission by a QD. The Light blue line represents a single-photon absorption event.[51]

If the energy possessed by the photon is exactly equal to that of the bandgap, the

excited electron will transfer from the valence band ("S0") to the lowest state in the

conduction band ("S1"). Photons that possess higher energies can excite electrons into

even higher energy states, such as "S2," from which the electrons will descend towards

the lowest state (S1 in this case) via a series of non-radiative internal conversions

between vibrational states. Once an electron reaches an excited state, it typically relaxes

back down to its original ground state, S0, through a radiative transition. Most often, this

occurs as a short-lifetime fluorescent transition in which the electron recombines with the

ground-state hole and a photon is released with energy equal to that of the bandgap. In

rare cases, electrons will undergo what are known as relatively forbidden transitions or

"intersystem crossings," in which electronic states will undergo a multiplicity change and

transition to a triplet state ("T1"). This multiplicity change occurs when the spin

orientation of the excited electron reverses; since a spin change is uncommon

(especially in light atoms), an intersystem crossing is relatively uncommon as well. From

this triplet state, an excited electron can either be further excited or undergo a long-lifetime radiative phosphorescent transition in which the electron very slowly relaxes through many vibrational states, releasing energy as light until reaching the initial ground state S0. Fluorescent emission is the most common type of gap transition for QDs by far, and is therefore the easiest to target.

In order to achieve enhanced emission from the QDs, the parent metasurface structure had to be tuned to match the emission wavelength of the QDs (Equation 4.5).

$$\lambda_{emission,QD} = \lambda_{MS\ gap\ resonance}$$

Equation 4.5 Tuning parameter criteria of the QD-MS system used to achieve single-photon emission enhancement.

By manipulating the MS fabrication parameters such as AgNC size, interparticle spacing, dielectric layer thickness, and others (discussed in Chapter 3), the resonance wavelength of the layered MS structure can be tuned to match the emission wavelength of the QD layer. The MS will then be excited with a monochromatic laser matching the absorption wavelength to induce emission from the QDs. Upon excitation with the laser, the MS generates an intense local field enhancement in the QD layer that lies between the AgNCs and the metal substrate. In response to incident light, each AgNC acts as an optical analogue of what are known as "optical patch antennae" (Figure 4.5), which scatter incoming electric waves via the excitation of effective magnetic currents.[46,47]
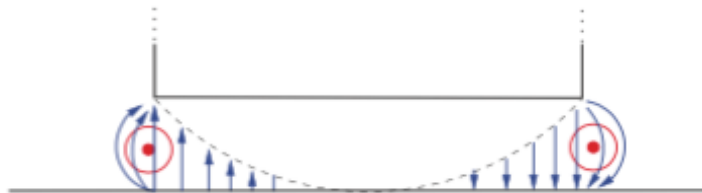
Figure 4.5 Representation of the electric and magnetic fields generated by an optical patch antenna in response to incident electromagnetic radiation.[46]

Similar to optical patch antennae, the AgNCs support a series of cavity-like resonances

in which the electromagnetic field is localized within the gap between the substrate and

the nanocubes (Figure 4.6). However, their local field structure is modified by the

plasmonic response of the metal's dielectric function and have the added feature of an

unnaturally large absorption efficiency that can be partially attributed to an

interferometric effect.[46] In plasmonic systems, field localization is correlated with local

field enhancement; in the context of this MS structure, the enhancement increases the

effective magnetic surface current that flows in response to the applied field, which in

turns increases the amount of "negated" electric field and therefore the amount of

incident light that is absorbed.[46] The absorption characteristics of this system is similar to

that of very shallow metallic gratings.[48]
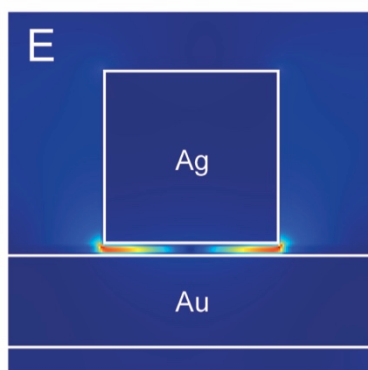
Figure 4.6 Visualization of the gap-plasmon electric field generated between the AgNC and the Au surface, similar to that of resonance modes seen from an optical patch antenna.[3]

In a way, the parent MS structure uses its high-absorbance to act as a "photonic

funnel" by funneling a larger proportion of outgoing photons into one specific direction

via an antenna effect. The increased direction experienced by the local population of

photons causes the intensity of their emission to increase, as it decreases the random

directional spread of outgoing photons generally seen from QDs in solution or on a

surface. The increased number of emission events again also experiences a

corresponding decrease in the overall emission lifetimes, increasing the "emission

density" and leading to an apparent increase in emission intensity. It is also possible to

tune the MS such that the fundamental mode aligns with the absorption wavelength of

the QDs, but the differences between using the MS to enhance absorption (and

corresponding emission) vs. enhancing emission directly are theoretically negligible for a

linear single-photon process.

4.4 Single-Photon Instrumentation

For the single-photon enhancement experiments, fluorescence measurements

were taken using a Renishaw InVia Raman microscope equipped with a 20x dry

objective and a 50 mWatt, 488 nm Argon ion photoluminescence laser. This system was

readily available and deemed sufficient to use for the single-photon experiments, as QD

emission was achievable by higher-energy excitation. The measurements performed

using this instrument were performed at 0.05% laser power with 10 second acquisition

times. Simulations were performed by finite-difference time domain (FDTD) method via

Lumerical FDTD Solutions software. Models used were typically 2D in order to reduce

computational time and make the implementation of periodic boundary conditions easier.

4.5 Single-Photon Enhancement Results

Simulated spectral results of the QD MS structure show the wavelength shift of

the fundamental plasmonic mode with changing AgNC sizes, as well as how these lie in

relation to the emission wavelength of the CdSe/ZnS QDs used for the single-photon

experiments (Figure 4.7).
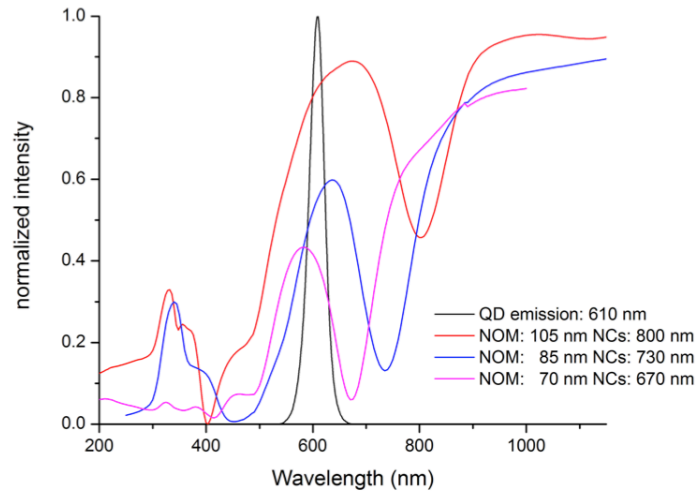
Figure 4.7 Simulated reflectance spectra of the QD MS overlaid on top of the emission spectrum of the QD layer.

As seen in the figure, increasing AgNC size led to redshifts in the fundamental resonance mode of the MS structure. This is due to increased out-of-plane coupling between the larger particles and the substrate, which increases the wavelength of confined light that is sustainable within the plasmonic gap. Red-emitting QDs with an absorption of ~ 590 nm had to be used, because their single-photon absorption peak was closest to the lowest tunable limit of the MS structure. Due to the constraints of tuning the surface as well as the size of the CdSe/ZnS QDs, the fundamental mode wavelength of the MS structure was not tuned to precisely the value of the QD absorbance. Due to this, the level of enhancement quantified was most likely not the theoretically maximum enhancement that was possible to achieve. However, the amount of emission enhancement seen was still significant despite the apparent spectral mismatch.

A tilted-plane SEM image of the MS structure containing the QD active layer reveals a somewhat incomplete but present monolayer between the AgNCs and the gold substrate, as outlined by the original structure schematic (Figure 4.8). Although this patchy QD monolayer somewhat inhibits the ability to quantitatively assess the per-particle enhancement, it does not inhibit the ability to quantitatively compare bulk measurements between the complete MS structure and the control structures.
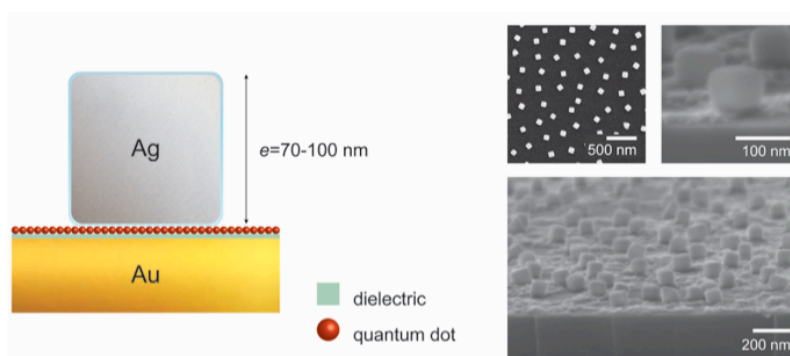
Figure 4.8 Schematic view (left) and SEM images (right) of the single-photon QD MS structure used to study QD enhancement characteristics.

The single-photon QD enhancement results for the complete metasurface, as well as for two different control structures, are illustrated in Figure 4.9A. The black curve represents a partial monolayer of CdSe/ZnS QDs with an emission wavelength of 610 nm on an HMDS-functionalized pure silicon wafer with no underlying metal film or present metal nanoparticles. This control structure was designed to show the unenhanced emission from a QD layer on a nonmetal substrate. The red curve represents a similar layer of QDs on an HMDS-functionalized silicon wafer, with a well-spaced LB film of AgNCs placed on top. This control structure was designed to show that the QD layer emission can be somewhat enhanced by the present of the AgNCs alone, as they will still respond to incident light with patch antenna behavior.
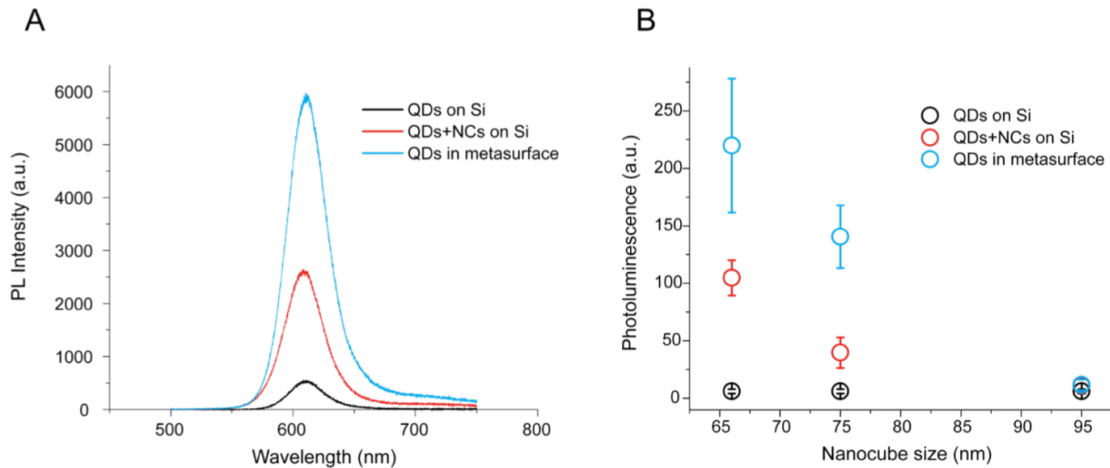
Figure 4.9 Figure detailing the enhanced emission profiles of the CdSe/ZnS QD layer (A), as well as the emission for the MSs fabricated with larger AgNCs (B). Enhancement decreases with increasing AgNC size due to fundamental mode shift.

However, due to the absence of the underlying gold film, out-of-plane coupling is significantly weakened; as a result, the enhanced electric field and enhanced emission as weaker as well. The blue curve represents the completed QD MS structure, which includes the underlying 50 nm gold film, the dielectric spacer layer, QD layer, and AgNC layer. The curve shows that enhancement from this complete structure is highest, showing an almost 12 times increase over just the QD layer alone.

Figure 4.9B shows the enhancement values for the structures fabricated using AgNCs of increasingly large sizes. As seen in the curve, enhancement of the QD emission decreases as the AgNC size increases. This is because increasing AgNC size shifts the fundamental mode wavelength progressively further away from the absorption wavelength of the CdSe/ZnS QDs; once the modes are fully out of alignment, the effect of the MS is negligible on the emission intensity of the QD layer.

Although Figure 4.9 adequately shows QD emission enhancement between the complete MS and the silicon control structures, it does not show any enhancement

different between incomplete structures of the same substrate type. Figure 4.10 shows a breakdown of emission profiles for a complete range of both silicon and gold-based MS structures. In both cases, AgNCs on either silicon or gold with no present quantum dots show no emission, as noble metal NPs do not emit in response to incident radiation. For silicon and gold structures, QDs placed between the substrate and AgNC layer both exhibit enhanced emission compared to just the QDs on the substrate alone. Interesting to note is that, although difficult to see, the QDs actually exhibit higher emission intensity when placed on silicon (without AgNCs) than on gold. This is because the gold film quenches the QD emission to some degree, whereas the silicon substrate does not.
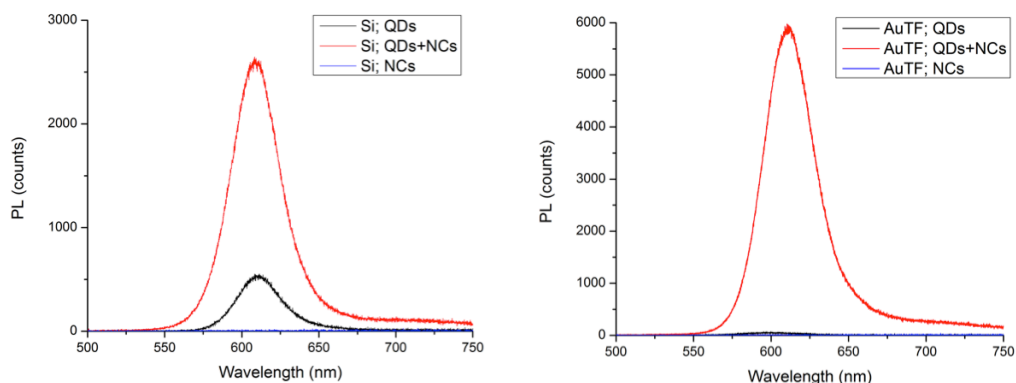
Figure 4.10 Enhancement profiles for silicon (left) and gold (right) substrate structures.

Similar (and more quantitative) emission enhancement results using a similar MS structure have been seen by Maiken Mikkelsen and her research associates in recent years.[49,50] Mikkelsen probed the emission of single AgNC junctions on gold films with an active layer of ruthenium dye-doped PAH/PSS polymer films. The placement of the dye molecules within the plasmonic junctions subjected them to intense electromagnetic field once the structures were illuminated. Similar to the emission of the QDs, enhanced emission was seen from the dye molecules, with rates sometimes exceeding three

orders of magnitude with high quantum efficiency and directional emission. However, the emission enhancements seen depended highly on the dipole orientation of the dye molecules within the gap, as well as the lateral position of the molecule under the nanocube. In the case of the QDs, enough quantum dots were present in the monolayer such that position was not nearly as large a factor in the overall enhancement. The QD enhancement was also much less than that of the dye, as it was calculated as an ensemble quality, rather than for a single particle.

The degree of emission enhancement seen in the single-photon experiments was typically on the order of at least an order of magnitude. Typically, excited monolayers of QD particles are often not bright enough to be seen with the naked eye. However, the emission enhancement caused by the MS structure was oftentimes sufficient to make this entirely possible. This opens up the possibility for the use of MS structures in optical devices that utilize fluorophores or other emissive particles, in sensing applications, photovoltaics, or other optical applications that may benefit from increased optical sensitivity.

Chapter 4 in part is currently being prepared for submission for publication of the material. Rozin, Matthew J,; Brown, Eric R.; Tao, Andrea R. The thesis author was one of the primary investigators and authors of this material.

CHAPTER 5: TWO-PHOTON ENHANCEMENT

5.1 Why is Two-Photon Enhancement Desirable?

As mentioned previously, quantum yield is generally defined as the number of times that a specific event occurs in a system per absorption of a photon. For fluorescent systems, QY is specified further to mean the ratio of photons emitted to photons absorbed. In a single-photon process, QY values can typically be very high depending on the type of fluorescent entity being studied. In comparison, nonlinear emission processes such as two-photon or multi-photon emission typically exhibit QY values that are a fraction of those seen for respective single-photon processes. This is primarily due to absorption probability differences and the resultant absorption cross-section differences between single-photon and two-photon absorption processes. Using a metasurface to enhance two-photon emission is one way to remedy some of these factors in order to get higher yields for nonlinear emissive processes.

Two-photon active molecules and particles are often used as contrast agents for molecular tagging, biological imaging, and medical treatment because the high-wavelength lasers used penetrate deeply into biological tissues without surface damage. However, due to the aforementioned absorption probability and absorption cross section, these lasers must be extremely powerful to be able to induce two-photon absorption and are typically expensive with a higher potential for sample destruction or patient injury. Using a device such as a small-scale colloidal MS could eliminate the need for extremely powerful lasers, as well as increase the sensitivity of many types of methods that utilize multi-photon processes.

5.2 Two-Photon Enhancement Mechanism

Similar to the case of single-photon enhancement, we must examine the way in which two-photon absorption and emission processes work in QDs and other fluorophores before we examine the way a colloidal MS can be tuned to enhance these processes. In single-photon absorption, an electron is excited to a higher energy state when an incident photon has energy equal to or greater than that of the semiconductor material bandgap energy. In the case of two-photon absorption, the energy of two photons must collectively match or exceed the bandgap energy in order for an excitation event to occur (Figure 5.1).
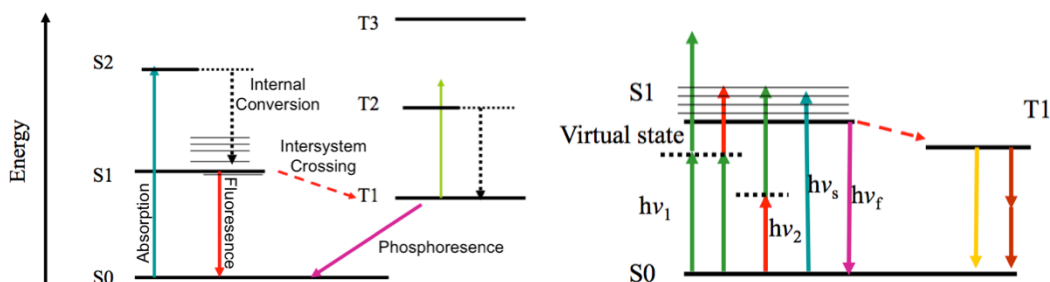
Figure 5.1 Band diagram for single-photon emission (left) compared to two-photon emission (right).[51]

In single-photon absorption, the necessary photon exists in a single physical and temporal location at the time of absorption. In two-photon absorption, two distinct photons, each with a unique physical and temporal location, must come together at the same time to constructively form the sum of their two frequencies (e.g. $v_1 + v_2$). The phrase "same time" refers to an interval of approximately 10^{-18} seconds.[51] Since this is a finite amount of time, this means that a photon of an energy (hv_1) less than the required bandgap energy can excite an electron to an intermediate "virtual state" between the ground state S0 and first excited state S1. This virtual state that lasts for 10^{-18} seconds

must then be further excited via the absorption of a photon of a second energy ($h\nu_2$) that is sufficient to further push the electron up to or past the excited state S1. From this point, excited electrons can recombine with their respective holes to cause single-photon fluorescent emission (at a lower wavelength than the two constituent photons), as well as transition to a triplet state T1 and radiatively transition back down the ground state S0 through other emissive processes.

Due to the fact that photons inherently operate on such small size and time scales, this interaction between two photons to produce this effect is comparably rare. In a single-photon process, transition probability depends on the polarization and beam orientation of the incident light, as well as the mathematical sum of transition possibilities between states. However, two-photon processes must take into account the small interaction volume at which two photons meet, as well as all of the individual components involved in a single-photon transition, but for both photons simultaneously. This leads to exceeding complex calculations for the two-photon transition probability of a fluorophore or QD, P_{if}, in which the transition from an initial energy state E_i to a final energy state E_f through an intermediate state E_k is subject to many unique factors (Equation 5.1).

$$P_{if} \cong \frac{\gamma_{if}}{\left[\omega_{if} - \omega_1 - \omega_2 - \vec{v} \cdot (\vec{k}_1 + \vec{k}_2)\right]^2 + \left(\frac{\gamma_{if}}{2}\right)^2} \cdot \left|\sum_k \frac{R_{ik} \cdot \vec{e}_1 \cdot R_{kf} \cdot \vec{e}_2}{(\omega_{ki} - \omega_1 - \vec{k}_1 \cdot \vec{v})} + \frac{R_{ik} \cdot \vec{e}_2 \cdot R_{kf} \cdot \vec{e}_1}{(\omega_{ki} - \omega_2 - \vec{k}_2 \cdot \vec{v})}\right| \cdot I_1 I_2$$

Equation 5.1 Two-photon absorption transition probability of a fluorophore or QD being excited by two light beams.[51]

The first term of Equation 5.1 describes the spectral line profile of the two-photon transition, the second term provides information on how wavelength, polarization, and beam orientation affect absorption probability, and the third describes the dependence of

two-photon absorption probability on the optical intensities of the incident beams.[51] The

meanings of the parameters in Equation 5.1 are listed in the following Table 5.1.

Table 5.1 Explanation of Parameters from Equation 5.1

Parameter	Meaning
ω_1, ω_2	Optical frequencies of each beam
e_i	Polarization vectors
k_i	Wave vectors
I_1, I_2	Optical beam intensities of each beam
γ_{if}	Homogeneous linewidth
v	Molecular velocity
R_{ik}, R_{kf}	Matrix elements for transitions between states (i = initial, k = intermediate, f = final)

The concept of transition and absorption probability is often wrapped up into the

much simpler concept of absorption cross section, which can provide a more intuitive

explanation of why two-photon events are much less common than single-photon

events. Generally, absorption cross section refers to the ultimate probability of an

absorption process occurring in a medium. CdSe QDs and other fluorophores typically

possess much larger absorption cross sections for single-photon events than for multi-

photon events (being on the order of 10^{-15} cm^2/atom for single photon and 10^{-50}

cm$^4 \cdot$s/atom for two-photon events),[52,53] which makes the occurrence of two-photon

absorption events much rarer and much more difficult to cause. Due to this, a

fluorophore that generates a certain number of emitted photons from *n* input photons

through a single-photon process needs *n • 10^6* as many incident photons to generate an

equivalent amount of emitted photons from a two-photon process. This is usually

accomplished by utilizing high-power lasers emitting high peak intensity light (such as

picosecond or femtosecond pulsed lasers) to achieve a high two-photon transition probability.[51] The use of MS can help to reduce this requirement, by again acting as a kind of "photonic net" or "photonic buffer" for a two photon process, increasing the amount of available photons of appropriate energy in proximity to the QD or fluorophore during excitation.

The theoretical principle for enhanced two-photon absorption is the same as that of single-photon absorption (see Section 4.3); the only apparent different difference is that the actual absorption mechanism for two-photon events is more complicated. In order to achieve enhanced emission from the QDs, the parent metasurface structure had to be tuned to match twice the absorbance wavelength of the QDs (Equation 5.2).

$$\lambda_{excitation,laser} = 2\lambda_{absorption,QD} = \lambda_{MS\ gap\ resonance}$$

Equation 5.2 Tuning parameter criteria of the QD-MS system used to achieve two-photon emission enhancement.

Unlike the single-photon emission metasurfaces that were tuned to red QDs with an absorption of ~ 590 nm, the two-photon experiment metasurfaces were tuned to accommodate blue QDs with a significantly bluer absorption at ~ 465 nm. This is because the available fluorescence microscope (discussed in the following section) had an excitation limit well before 1180 nm, which would be approximately the two-photon absorption wavelength of the red QDs. The blue QDs also possessed a two-photon absorption that the MS structure could be tuned to without dramatically altering the MS design or structure parameters. Figure 5.2 shows the range of two-photon MS tunability for a typical range of QDs, as well as the experimentally and theoretically determined possible resonance wavelengths of the NOM parent structure.
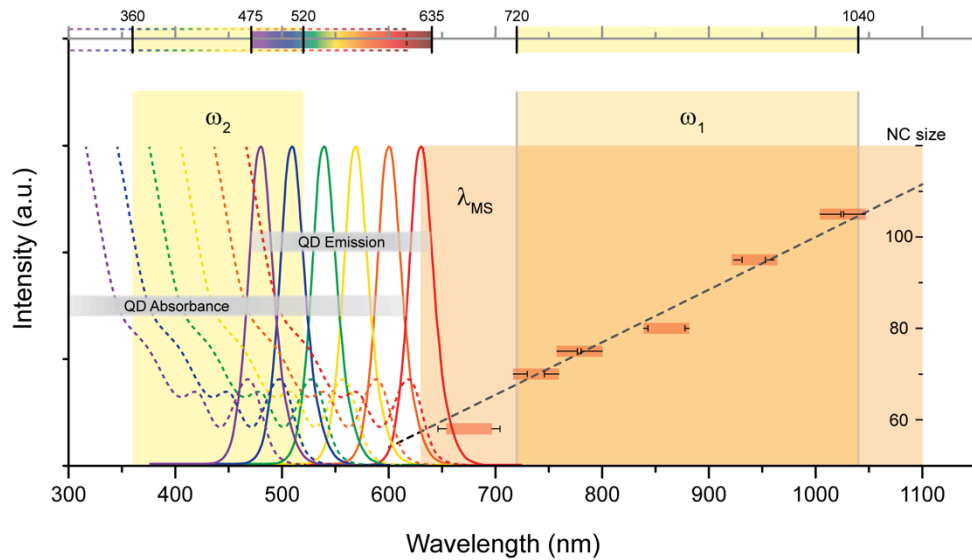
Figure 5.2 Diagram exhibiting the ranges of CdSe QD absorption and emission, as well as the tunability of the MS. Two-photon enhancement is possible for any QD with absorption in the ω_2 range with MSs that lie within the ω_1 range.

Similar to the single-photon case, it is also possible to enhance both the absorption and emission of the two-photon case. Unlike in the single-photon case, the chosen enhancement mechanism matters significantly in the two-photon case. Since the two-photon absorption cross section is already comparatively low, tuning the MS resonance to the QD emission wavelength does little in the way of enhancing the emission intensity since the QD experiences few initial absorption events to begin with. Tuning the metasurface to the two-photon absorption wavelength leads to enhanced absorption and consequently enhanced emission of the two-photon process overall. Thus, the overall achievable enhancement factors for a two-photon process are larger when the absorption is enhanced.

The overall idea of is that the use of a metasurface structure will artificially increase the QD two-photon cross section, ultimately increasing the two-photon

transition probability and therefore leading to enhanced emission intensity from two-photon processes. In a way, the parent MS structure uses its high-absorbance to act as a "photonic funnel" by capturing a larger proportion of incident photons, and then confining them to the local space in which the QDs reside. The increased local population of photons (that manifests as a local field enhancement) provides more photons with which the QDs can interact, leading to a corresponding increase in the amount of two-photon absorption events in the QD semiconductor medium. The increased number of absorption events again leads to a corresponding increase in the amount of emission events, leading to an apparent increase in emission intensity.

5.3 Two-Photon Instrumentation

For the two-photon enhancement experiments, fluorescence measurements were taken us a Leica SP5 scanning confocal microscope equipped with a 20x dry fluorescence objective. This microscope was equipped with several different lasers: those that were used for these experiments were a continuous wave 50 mW 405 nm diode laser and a 100 fs-pulsed 2.5 W tunable Ti:sapphire laser with an available tuning range of 690 – 1040 nm. The ability to tune this laser to different wavelengths was very desirable to test a variety of structures with different fabrication parameters. Two-photon excitation wavelength-varying scans were conducted across the full 690 – 1040 nm range with a 1 nm step size (smallest possible for excitation) at 10% power transmission. Two-photon emission wavelength-varying scans were conducted at an excitation wavelength of 934 nm (roughly twice the absorbance of the blue QDs, as well as twice the wavelength of the MS resonance cavity) across a range of 410 – 780 nm with a 3 nm step size (smallest possible for emission), 5 nm collection bandwidth, and 70% power transmission. Both sets of measurements on the Leica instrument used a GaAsP hybrid

PMT detector manufactured by Leica. Scattering optical spectra were taken using a spectrometer-coupled Nikon optical microscope with a 50x brightfield objective.

5.4 Two-Photon Enhancement Results

The construction of the QD MS was slightly different for the two-photon enhancement experiments as compared to the single-photon enhancement experiments. This was to incorporate a slightly different type of QD (that was purchased rather than synthesized), as well as to tune to a much lower wavelength. Larger AgNC films were placed on top of a near-monolayer of QDs that rested on a 1-HDT SAM, which all rested on an optically thick 75 nm gold thin film (Figure 5.3).
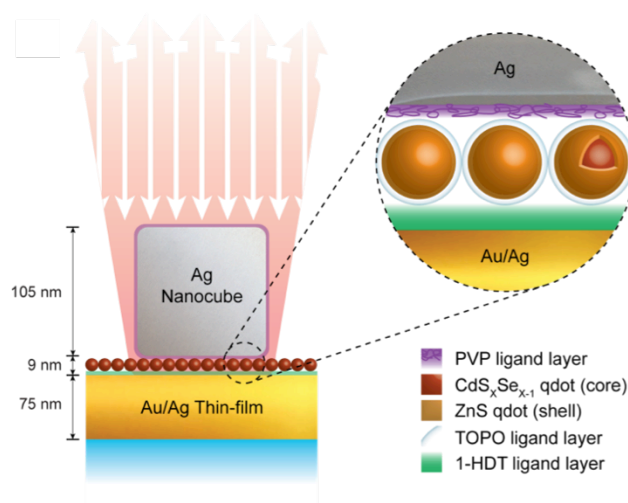
Figure 5.3 Schematic of the fabricated QD metasurface structure used to achieve two-photon emission enhancement. Inset shows a close-up view of the QDs contained within the MS resonance gap.

Absorption and fluorescence spectra of the blue-emitting colloidal QD solution show a very narrow absorption curve at 467 nm and similarly narrow emission curve at 488 nm (Figure 5.4A). The fluorescence of the QD layer shifts to a slightly larger wavelength once the QDs are configured into a 2D near-monolayer film. This is most likely due to

either a small amount of particle ripening occurring due to close particle proximity on the

substrate surface, or some effect caused by the substrate itself. Simulated scattering

spectra of a MS structure containing these fabrication parameters (105 nm AgNCs, 9 nm

gap, 75 nm gold film, etc.) predict a fundamental plasmonic gap resonance wavelength

at exactly 934 nm, or twice the absorbance wavelength of the CdS_xSe_{1-x}/ZnS QDs in

colloidal solution as desired by the design parameters of the experiment (Figure 5.4B).

Scattering spectra taken of the assembled MS using the spectrometer-coupled Nikon

microscope experimentally show this same fundamental resonance wavelength. The

apparent noise in the experimental signal in the 400 – 500 nm regions as well as the 900

– 1000 nm regions stems from the limitations of the spectrometer on the visual

microscope. Although the signal is noisy, both the spectra seemed to match reasonably

well for the purposes of the experiment.
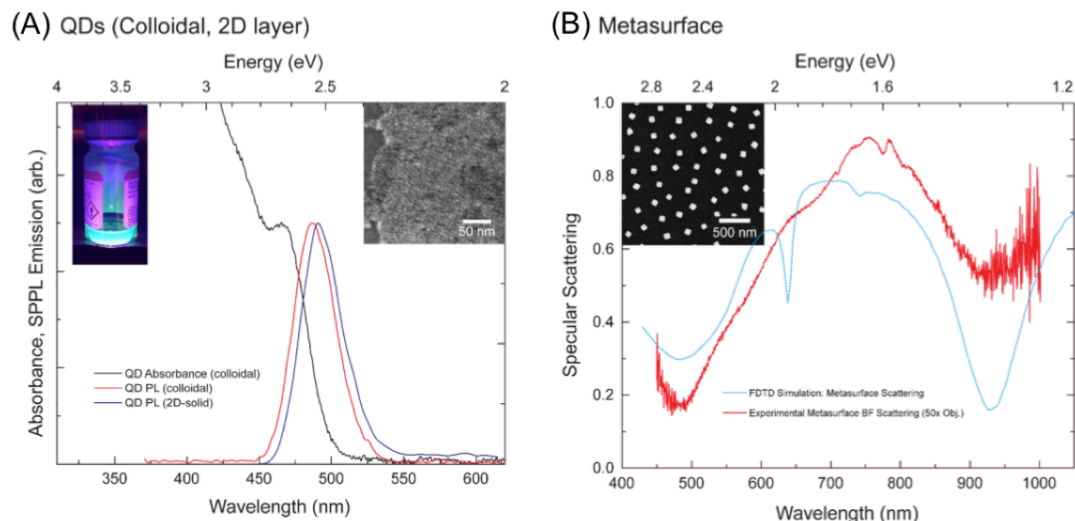
Figure 5.4 A) Absorption and fluorescence spectra of the CdS_xSe_{1-x}/ZnS QDs use for two-photon enhancement. Left inset: photo of the QDs under UV illumination, right inset: SEM image of QD film. B) Simulated and experimental scattering spectra of the QD-MS. Inset: SEM image of the uniform AgNC array layer.

Photoluminescent excitation (PLE) measurements of the QD/MS structure and the QD layer-on-Si control sample were performed by slowly scanning the excitation laser from 690 to 1040 nm and measuring the resultant absorption of the QD layer. In Figure 5.5, the black curve represents a PLE measurement of a 2D QD layer on a plain Si substrate, whereas the red curve represents a PLE measurement of the complete QD-MS structure. These curves show a rather large enhancement of QD layer absorption from the QD/MS structure, which exhibited almost two orders of magnitude more absorption than just the QD layer on Si. The ratio of these two curves is shown by the blue curve, which demonstrates that the enhanced absorption effect occurred most noticeably at approximately twice the single-photon absorption wavelength (934 nm), which also corresponded to the fundamental resonance frequency of the metasurface structure. The sharp drop-off just past 950 nm is due to the fact that the photons supplied to the QD layer no longer possess enough energy to incite two-photon absorption. This PLE data suggests that the MS structure is causing two-photon absorption enhancement; however, the lack of a clear absorption peak on the black QD-only curve leaves it unclear whether or not the QD layer (and not simply the MS structure itself) is experiencing enhanced absorption.
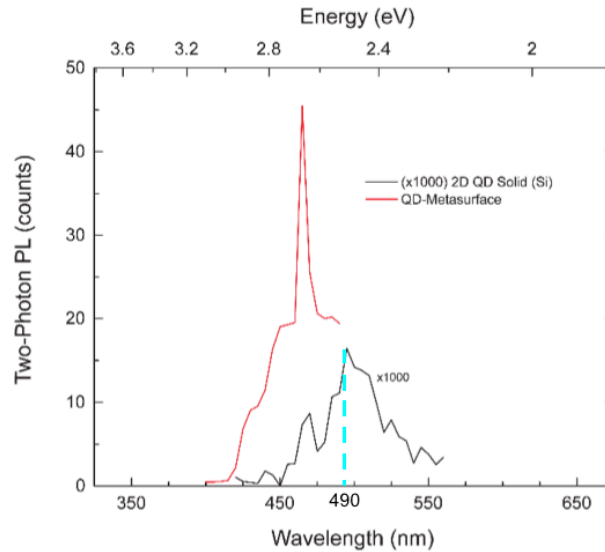
Figure 5.5 PLE curves for the QD-on-Si sample (black curve) and complete QD-in-MS structure (red) that demonstrate enhanced absorption. The blue curve is a simple ratio of the two curves.

Photoluminescence measurements of the QD-MS structure and control sample (Figure 5.6) show a similar behavior. The red curve represents emission from the QD-MS under 934 nm excitation, and the black curve represents emission from a QD layer on Si at this same excitation wavelength. Again, the QD-MS signal enhancement here is on the order of over three orders of magnitude compared to the QD layer on Si. The overall signal measured was greater in the case of the MS structure, but pinpointing the exact source of the enhanced signal was complicated by the presence of the sharp peak at approximately 450 nm. Whereas the black curve showed a more clear peak corresponding to the emission wavelength of the QD layer (490 nm), the sharp peak on the red curve did not appear to correspond to QD emission, as the emission wavelength is almost 40 nm blueshifted from the expected emission wavelength of the QD layer. It is more likely that this peak at 450 nm corresponds to a second harmonic generation (SHG) effect coming from the metasurface structure directly.
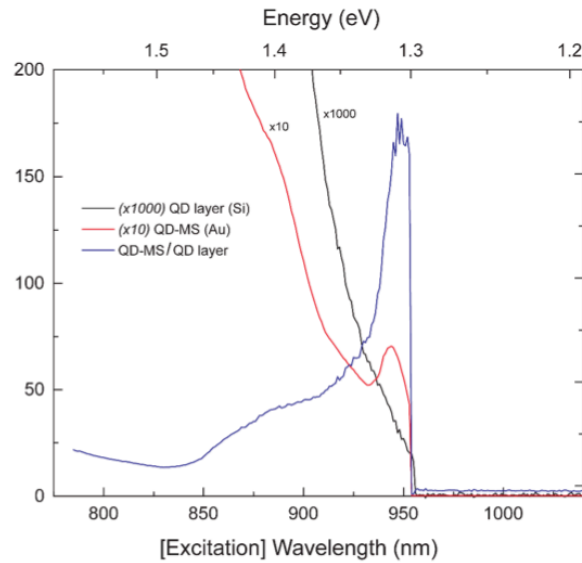
Figure 5.6 Photoluminescence measurements of the QD-MS structure and the QD-on-Si control sample.

Second harmonic generation is a nonlinear second-order optical process in which two photons of a given frequency (corresponding to the frequency of an incident light source) are converted into a single photon with twice the frequency (or half the wavelength) of the original photons.[54] This effect increases nonlinearly with electric field amplitude and can be heavily enhanced by the presence of plasmonic nanostructures, such as the metasurface structure used to enhance QD emission in these experiments. It has been reported that reflected SHG intensity increases by several orders of magnitude when incident light angle permits the launching of surface plasmon polaritons, meaning that plasmon polaritons have the ability to increase nonlinear signals.[54] Due to the effects of LSPR enhancement, SHG from plasmonic nanostructures is actually significantly higher than has been seen from even the best chromophore samples.[54] This effect is most clearly observed when the wavelength of incident light

matches the resonant wavelength of a LSPR, as is seen in our measurements. One thing that differs between the SHG seen from the MS structure and those seen from other tested structures, is that the SH peak seen in Figure 5.6 lies at a wavelength less than half of the incident light wavelength. This may be explained by the fact that SH emission spectra are much more complex than their corresponding linear spectra, since multiple different resonances can occur simultaneously.[54]

Two main pieces of evidence suggest that this SHG peak is a direct result of the MS structure itself and not due to the presence of the QD nanocrystals. One piece is illustrated by Figure 5.7, which shows that the SHG peak is directly correlated to incident light wavelength.
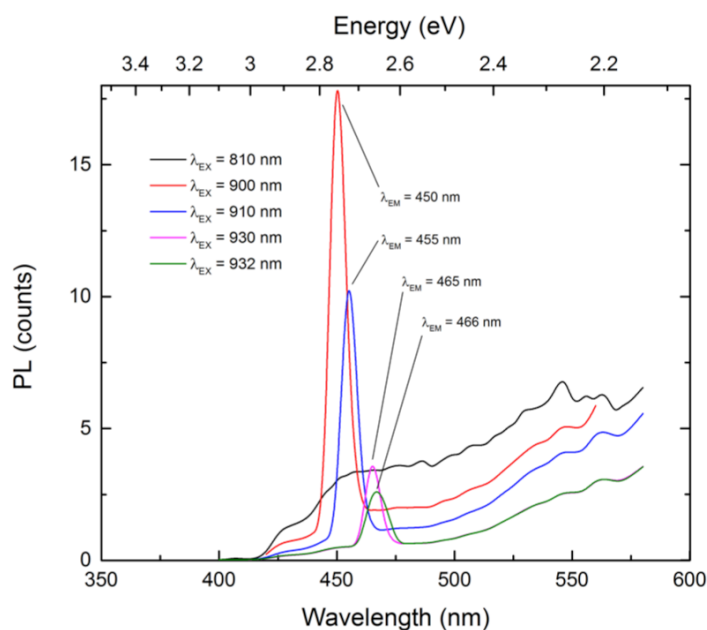
Figure 5.7 Photoluminescence spectra showing increasing blueshift of the SH wavelength with decreasing incident light wavelength.

As the incident light wavelength is decreased, there is a directly corresponding decrease in the SH peak wavelength as well. There was also a corresponding increase in SH emission intensity, but this was most likely due to the fact that the tunable laser system used tended to vary in power output at different wavelengths. Since the SH peak seems to move in direct relation to the changing incident light and has little to no relation to the absorption or emission of the QD layer, it is seems likely that the SHG effect is caused by the metasurface structure directly. A second piece of evidence is that several control samples were made in which the QD layer was replaced by a thin aluminum oxide layer of near-identical thickness. This SHG effect was seen in these samples as well, despite the complete absence of any QD nanocrystal particles (Figure 5.8B).

Along with the appearance of this SHG effect, the metasurfaces exhibited a white light generation (WLG) effect in the form of what is known as a white light supercontinuum throughout all of the attempted two-photon enhancement experiments.[55] The spectra shown in Figure 5.8 reveal this WLG effect as well as a few of the metasurface structure parameters that appear to affect both SHG and WLG. The emission intensity of both phenomena changed in response to the absence of QD material (Figure 5.8A) and changes in excitation power (Figure 5.8B,C), and spectral shape changed in response to changes in metasurface gap spacing (Figure 5.8C). One notable feature about all of the WLG spectra is that the white light signals exhibit small fluctuations at identical spectral locations for all of the different metasurface samples. This could possibly be attributed to a Fabry-Perot resonance between different elements of the sample.[55] It is somewhat unknown at this point what causes this effect within plasmonic nanostructures, and thus explanations as to why it may exist here are limited.

It seems likely that this SHG/WLG effect is occurring somewhat exclusively, bypassing the QD absorption almost completely and overshadowing any emission signal from the QDs themselves. Due to these effects, conclusive evidence of two-photon emission enhancement using this uniform colloidal metasurface was not obtained. It may be possible to use single particle measurements to better quantify any enhancement, but this experiment was not conducted due to time constraints.

Chapter 5 in part is currently being prepared for submission for publication of the material. Rozin, Matthew J,; Brown, Eric R.; Tao, Andrea R. The thesis author was one of the primary investigators and authors of this material.
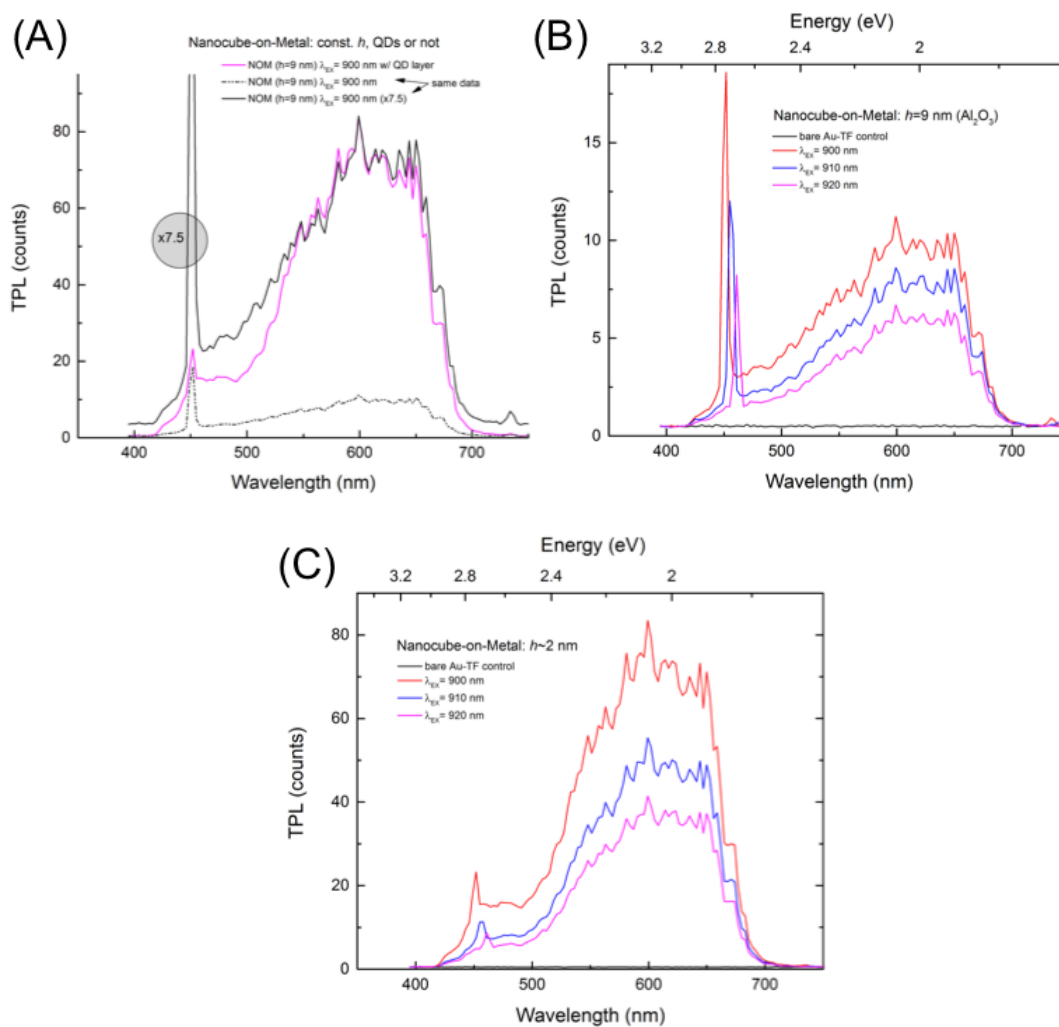
Figure 5.8 Fluorescence spectra showing the SHG and WLG effects seen for the colloidal metasurface enhancement structures.

CHAPTER 6: FUTURE WORKS AND APPLICATIONS

6.1 Two-Photon White Light Generation

As mentioned before, in the process of investigating enhanced two-photon emission using the highly uniform colloidal metasurface structures, an interesting optical effect was observed when the metasurface structure was placed under the high-power two-photon laser. Under large excitation wavelengths (generally greater than 800 nm), the metasurface structure appeared to absorb a single wavelength of photon and emit a broad spectrum of photons in the form of white light along with a second harmonic peak generated at exactly half of the excitation wavelength. This white light generation process was present throughout most of the two-photon experiments, and seems to be rooted in the nature of the particle-substrate interactions.

Some of the earliest work investigating WLG from optical antennas was performed by Mühlschegel and his research partners while exploring strong field enhancement in the gaps between nanostructures fabricated by focused ion beam lithography.[55] They noticed that, upon illumination with a picosecond-pulsed laser source, the antenna gaps would generate white light super continuum radiation (Figure 6.1) and the antenna arms themselves would generate two-photon photoluminescence.
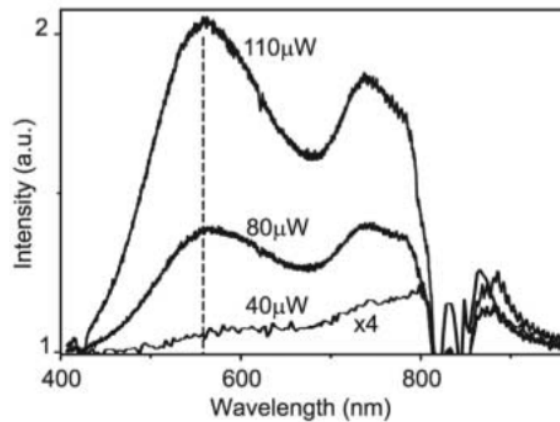
Figure 6.1 White light super continuum radiation emitted from the junction gap of a rectangular plasmonic optical antenna for different excitation powers.[55]

Although they conceded that the mechanisms underlying the WLG phenomenon in their system were not well understood, they largely concluded that the strong field concentration in the antenna gap suggests that WLG occurs primarily in the underlying substrate material, or possibly in particles unintentionally present within the gap.[55]

A WLG phenomenon very similar to that seen in these experiments was seen by Kaspar Ko and his research associates when studying the nonlinear optical responses of repeating arrays of gold bowtie antennas.[56] Ko constructed arrays of gold bowtie antennas on ITO and glass substrates (Figure 6.2), and illuminated them with a femtosecond-pulsed Ti:sapphire laser similar to that used in our experiments.
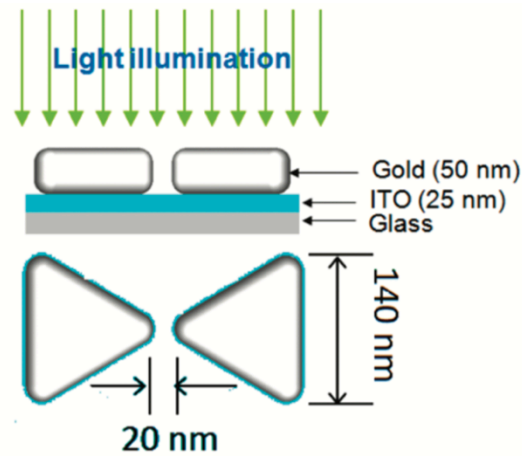
Figure 6.2 Au bowtie nanoantenna structure used to achieve white light super continuum generation via irradiation with a two-photon laser.[56]

Ko noted that the array would experience second harmonic generation at a wavelength exactly half of the excitation wavelength, as well as a white light continuum generation (Figure 6.3). The white light continuum exhibited small fluctuations at identical spectral locations for all arrays and incident polarizations, similar to that seen with the AgNC metasurface (Figure 6.4), which could possibly be attributed to a Fabry-Perot resonance between different elements of the sample.[55] It was also observed that SHG was largely

enhanced in the proximity to the sharp tips of the bowtie antenna, an effect also seen from the AgNC metasurface. Overall spectra shape appeared to be unique to incident polarization as well.[56]
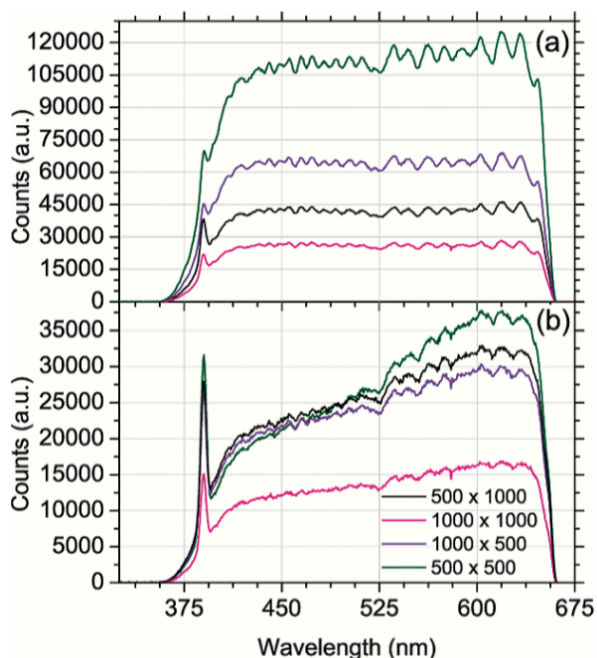
Figure 6.3 Fluorescence spectra showing the WLG phenomenon from an array of Au bowtie antennas illuminated with a high-power two-photon laser.[56]

In the two-photon experiments from this work, WLG was observed in all of the colloidal MS structures, regardless of QD layer presence, when placed under two-photon excitation (Figure 6.4A). WLG from the uniform nanoparticle array metasurfaces was often so strong that it often overwhelmed the emission signal from the QD layer, which may necessitate single particle two-photon measurements to attempt to obtain enhancement values for the QD layer without any signal from the MS structure. As seen in Figure 6.4, the specific features WLG phenomenon were a function of the colloidal metasurface construction parameters. SHG intensity changed in response to the

absence of QD material (Figure 6.4A), WLG intensity changed in response to changes in excitation power (Figure 6.4B,C), and spectral shape changed in response to changes in gap spacing (Figure 6.4C). Future works would explore the mechanisms behind the WLG phenomenon in this structure, as well as try to quantify the tuning parameters that can be used to shape the WLG response of the surface.
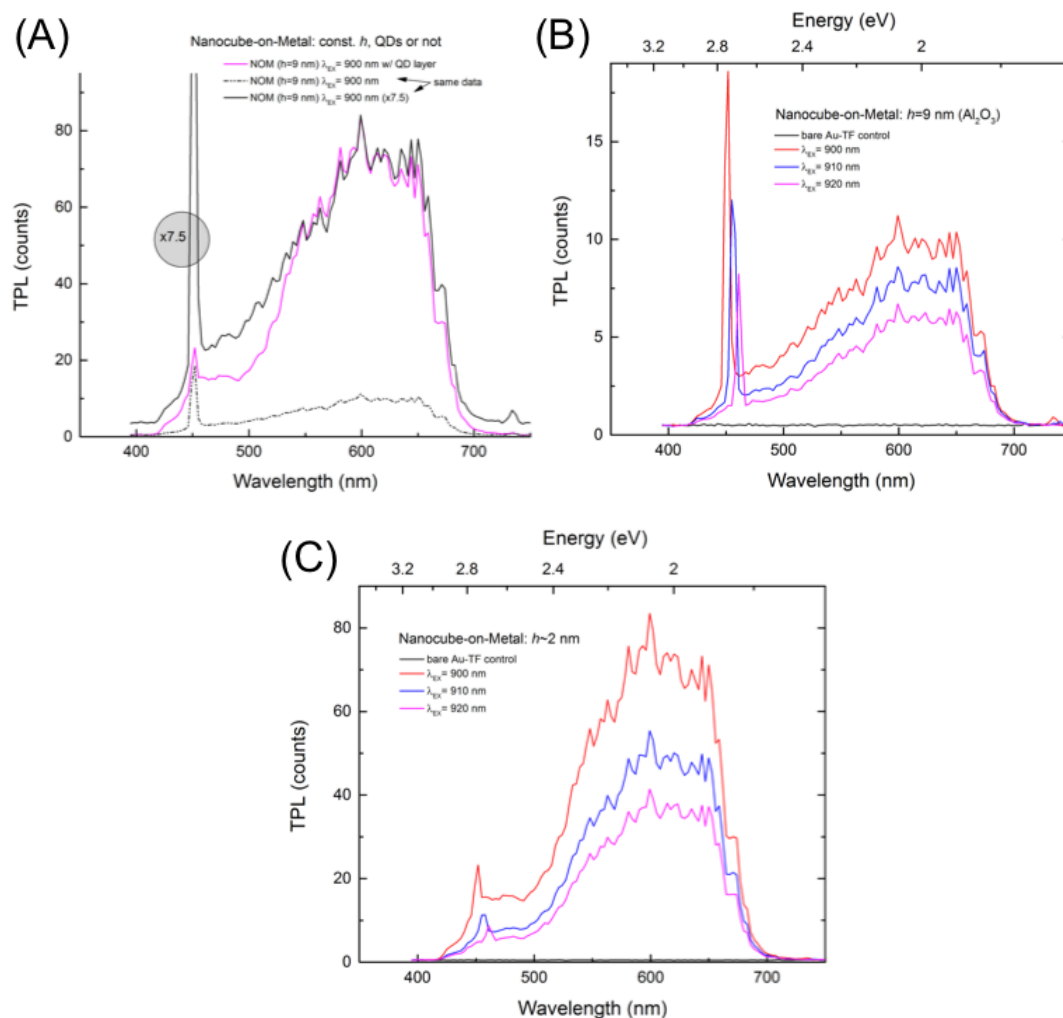
Figure 6.4 Fluorescence spectra showing the WLG effect seen for the colloidal metasurface enhancement structures. (A) WLG appears regardless of QD presence, (B) WLG intensity in response to excitation intensity, and (C) spectra shape change with different gap height.

Further investigation into this effect would need to be conducted in order to determine whether or not the efficiency of this SHG/WLG phenomenon is comparable to or better than that seen in other reports before more extensive research on this structure would be conducted. A different set of experiments than those performed would need to be conducted in order to more quantitatively demonstrate improved efficiency. A white light super continuum generating surface with nanoscale features that can be easily tuned through bottom-up assembly methods would be a novel way to approach white light generation from laser sources, and could perhaps be a useful device to many branches of photonics and electrons science. A phenomenon such as this could even be used to create functional devices, such as thin film white-light light-emitters, which could help usher in a new generation of solid-state lighting.

6.2 Metasurface Organic Photovoltaics

A second type of active layer that could be incorporated into this colloidal metasurface structure is a photoactive polymer, such as a number of popular polythiophene compounds commonly used in the organic photovoltaic (OPV) device industry. High-efficiency OPV devices is a somewhat new area of study that has become extremely popular within the last two decades, and is currently one of the most researched topics in the field of optoelectronics and sustainable energy with thousands of new papers being published every year. Most of these studies focus on attempting to create more efficient polymers and dopants to serve as active layers within a somewhat standardized device construction, in order to improve the collection efficiency of the device as a whole (Figure 6.5).
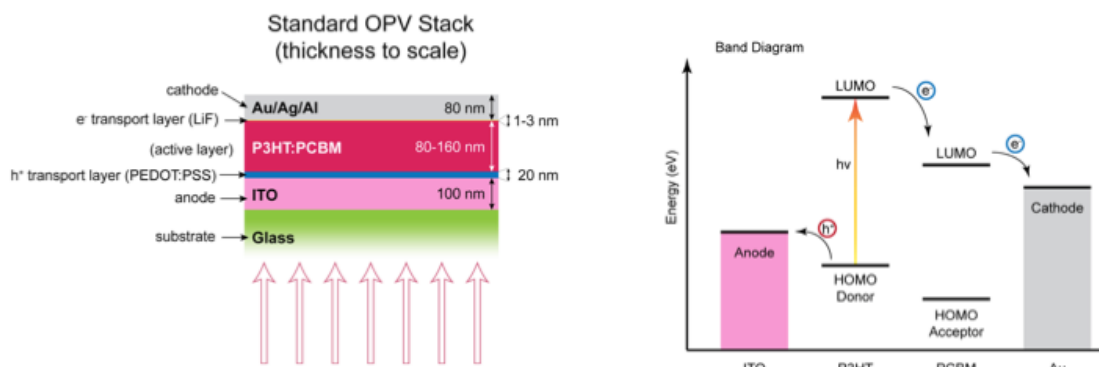
Figure 6.5 Schematic showing a typical device construction for an organic photovoltaic cell fabricated using common materials (left), as well as a simple diagram illustrating electron-hole separation and harvesting in the active layer upon irradiation (right).

The use of metal plasmonic nanoparticles to improve photovoltaic devices has been proposed in recent years as a way to improve the absorption capabilities of active layers without modifying the active layer composition itself. Metallic nanoparticles can be used as sub-wavelength antennas in which incident light is trapped in an active region by the excitation of localized surface plasmons on the nanoparticle surfaces (Figure 6.6A).[43] The excited nanoparticles' near field causes the creation of electron-hole pairs in the absorbing semiconductor material, ultimately improving the collection efficiency. By incorporating a standard OPV polymer active layer into the plasmonic gap of our colloidal metasurface and then modifying the MS structure such that it functions as an OPV cell, it should be possible to achieve both enhanced absorption and electron-hole pair generation Figure 6.6B). By examining the proposed metasurface OPV structure (Figure 6.6B), parallels can be seen between both the MS enhancement structure used throughout the QD layer emission enhancement experiments as well as the standard OPV structure in Figure 6.5. In the MS OPV structure, the topmost gold layer would

serve as both the OPV device top electrode and the noble metal substrate with which

the AgNCs will form a plasmonic gap region.
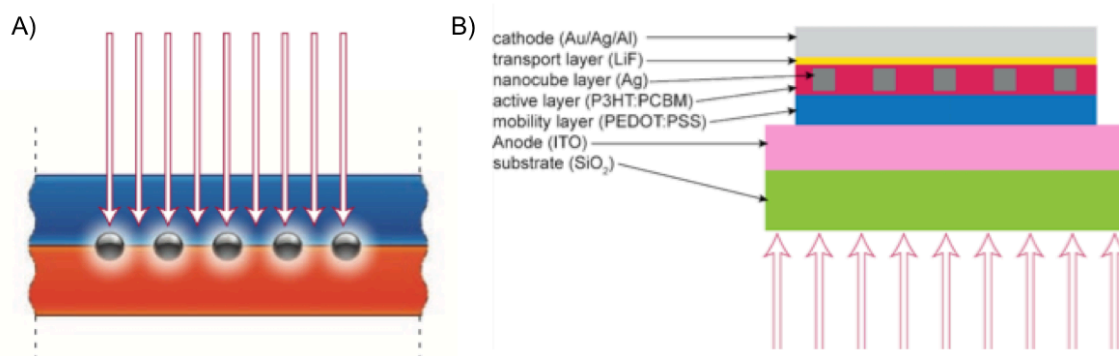
Figure 6.6 A) Illustration demonstrating the incorporation of plasmonic nanoparticles into an active layer region to improve OPV efficiency.[43] B) Metasurface-based OPV structure with silver nanocubes incorporated into the active layer region.

The LiF layer would serve as both the spacer layer and an electron transport layer, and

the AgNCs would be embedded into a poly(3-hexylthiophene) (P3HT) active layer doped

with phenyl-C61-butyric acid methyl ester (PCBM). A poly(3,4-

ethylenedioxythiophene) polystyrene sulfonate (PEDOT:PSS) layer would serve

as the hole transport layer, as is standard in most OPV cells. Finally, a thin layer

of indium tin oxide (ITO) on a glass substrate will serve as the transparent bottom

electrode and device substrate.

By combining the absorbing metasurface structure with a common OPV

type structure, it may be possible to achieve highly efficient OPV devices by

combining the effects of increased metasurface-based enhanced absorption and

plasmonic nanoparticle electron-hole generation. Most of this device could be

constructed using LbL assembly techniques, and would possess all of the

benefits typically possessed by OPV devices. One possible downside may be increased device thickness: current thin-film OPV devices only need active layer thickness on the order of bout 10 nm; however, implementing AgNCs into the active layer could potentially increase this thickness to the order of 100 nm. If the incorporation of the MS structure provided greatly increased power generation, then this drawback could be well worth it. An OPV device with an efficiency and power density that rivals modern silicon crystal solar cells could help to revolutionize the solar industry and increase the feasibility of solar power generation on a global scale.

CHAPTER 7: CONCLUSION

7.1 Overview

This work was able to study the effects of layer-by-layer assembled highly uniform colloidal metasurface structures on the absorption and emission enhancement of semiconducting quantum dot active layers. By varying the metasurface construction parameters and quantum dot nanocrystal sizes, alignment of the metasurface fundamental resonance mode within the absorption ranges of different sizes of quantum dots was possible. This allowed the quantum dots suspended within the metasurface cavity to be exposed to highly intense localized electric field via plasmonic resonance effects, which ultimately improved their emissive properties compared to a control sample.

Clear indications of linear single-photon enhancement were seen from the first round of experiments, in which the emission intensity of a quantum dot layer within the colloidal metasurface structure was many times larger than that of a quantum dot layer on a plain silicon substrate. It was observed that the greatest levels of emission enhancement resulted from "complete" metasurfaces in which silver nanocubes coupled with an underlying gold film, rather than with a silicon substrate. It was also observed that close proximity of the metasurface fundamental resonance mode to the absorption wavelength of the quantum dot film was necessary to achieve any measurable enhancement.

Indications of nonlinear two-photon enhancement were decidedly less clear due to the unexpected presence of second harmonic generation and white light supercontinuum generation that was emitted by the metasurface directly. The signal intensity of this white light generation was often much greater than any expected from two-photon emission of the quantum dot layer, and existed within the same spectral

region at which the two-photon emission wavelength was expected. Although this presence of this phenomenon made it difficult to achieve a clear indication of two-photon absorption/emission enhancement, this enhancement should still exist in some measurable fashion.

Further investigations into the white light generation phenomenon revealed that the generation itself was a product of the metasurface structure alone, as the presence of a quantum dot layer had no noticeable effect on the white light emission profile. However, this emission was profile was directly affected by incident light intensity, as well as plasmonic gap height. Further investigation into this effect would be necessary to determine its underlying mechanism, as well as a more complete list of the metasurface parameters that affect it.

7.2 Applicability of Colloidal Metasurfaces

There are several general instances in which layer-by-layer, highly uniform colloidal metasurfaces could be applied. In terms of research, these metasurfaces could be used as SERS substrates to study thin surfaces, molecules, or even two-dimensional crystal structures. They could also be used to study the physical nature of fluorescent or phosphorescent particles, most notably the ways in which their absorptive and emissive properties are affected by highly concentrated electric fields. Generally, these metasurfaces could be used to examine entities and systems that are otherwise difficult to examine due to low output signals. In terms of devices, these metasurfaces could be used as components of inorganic and/or organic photovoltaic devices, solid state lighting devices, efficient digital interfaces, and many more. Overall, colloidal metasurfaces are worth studying due to their innate flexibility of construction and wide potential for use and integration.

REFERENCES

[1] Greg Emmerich, UW Madison, M.S. in Biotechnology Program, Early Drug Development Class. Nov 16, 2012.

[2] Rycenga, M., Cobley, C.M., Zeng, J., Li, W., Moran, C.H., Zhang, Q., Qin, D. and Xia, Y. Controlling the synthesis and assembly of silver nanostructures for plasmonic applications. *Chem. Rev.* **111**, 6 3669–3712 (2011).

[3] Rozin, M.J., Rosen, D.A., Dill, T.J., and Tao, A.R. Colloidal metasurfaces displaying near-ideal and tunable light absorbance in the infrared. *Nat. Comm.* **6**, 7325 1-6 (2015).

[4] Hyuk, S., Lee, Y., Wiley, B., and Xia, Y. Large-scale synthesis of silver nanocubes: the role of HCl in promoting cube perfection and monodispersity. *Ang. Chem.* **44**, 14 2154-2157 (2005).

[5] Lee, S.Y. (2012). "Assembly of Silver Nanocube Clusters and Tuning of Surface Plasmon Resonances for Surface-Enhanced Raman Scattering," *Digital Repository University of Maryland*, pp 1-133.

[6] Tao, A.R., Habas, S., and Yang, P. Shape control of colloidal metal nanocrystals. *Small* **4** (3), 310-325 (2008).

[7] Pors, A., Albrektsen, O., Radko, I., and Bozhevolnyi, S. Gap plasmon-based metasurfaces for total control of reflected light. *Sci. Rep.* **3**, 2155 (2013).

[8] Tao, A.R., Sinsermsuksakul, P., and Yang, P. Tunable plasmonic lattices of silver nanocrystals. *Nat. Nano.* **2**, 435-440 (2007).

[9] Murphy, C.J. (2002). Optical sensing with quantum dots. *Analytical Chemistry.* 520A-526A.

[10] Zhang, C., Yeh, H., Kuroki, M., and Wang, T. Single-quantum-dot-based DNA nanosensor. *Nat. Mater.* **4**, 826-831 (2005).

[11] Freeman, R. and Willner, I. Optical molecular sensing with semiconductor quantum dots. *Chem. Soc. Rev.* **41**, 4067–4085 (2011).

[12] Xing, Y. and Rao, J. Quantum dot bioconjugates for in vivo diagnostics & in vivo imaging. *Cancer Biomarkers* **4**. 307-319 (2008).

[13] Resch-Genger, U., Grabolle, M., Cavaliere-Jaricot, S., Nitschke, R. and Nann, T. Quantum dots versus organic dyes as fluorescent labels. *Nat. Meth.* **5**, 9 763-775 (2008).

[14] Anikeeva, P., Halpert, J., Bawendi, M. and Bulovic, V. Quantum dot light-emitting devices with electroluminescence tunable over the entire visible spectrum. *Nano Lett.* **9**, 7 2532-2536 (2009).

[15] Huffaker, D.L., Park, G., Zou, Z., Shchekin, O.B. and Deppe, D.G. 1.3 μm room-temperature GaAs-based quantum-dot laser. *App. Phys. Lett.* **73**, 18 2564-2566 (1998).

[16] Richardson, J., Björnmalm, M., and Caruso, F. Technology-driven layer-by-layer assembly of nanofilms. *Science* **348**, 6233 aaa2491 (2015).

[17] Tan, B.J.Y., Sow, C.H., Koh, T.S., Chin, K.C., Wee, T.S., and Ong, C.K. Fabrication of Size-Tunable Gold Nanoparticles Array with Nanosphere Lithography, Reactive Ion Etching, and Thermal Annealing. *J. Phys. Chem. B* **109**, 11100-109 (2005).

[18] Min, Y., Akbulut, M., Kristiansen, K., Golan, Y., and Israelachvili, J. The role of interparticle and external forces in nanoparticle assembly. *Nat. Mat.* **7**, 527-538 (2008).

[19] Tseng, A., Notargiacomo, A., and Chen, T.P. Nanofabrication by scanning probe microscope lithography: A review. *J. Vac. Sci. Tech.* **23** (3), 877-894 (2005).

[20] Morimoto, H., Sasaki, Y., Saitoh, K., Watakabe, T., and Kato, T. Focused ion beam lithography and its application to submicron devices. *Microelectronic Engineering* **4**, 163-179 (1986).

[21] Lenggoro, I.W., Lee, H.M., and Okuyama, K. Nanoparticle assembly on patterned "plus/minus" surfaces from electrospray of colloidal dispersion. *Journal of Colloid and Interface Science* **303**, 124-130 (2006).

[22] Santhanam, V. and Andres, R.P. Microcontact Printing of Uniform Nanoparticle Arrays. *Nano Letters* **4** (1), 41-44 (2004).

[23] Grzelcak, M., Vermant, J., Furst, E.M., and Liz-Marzán, L.M. Directed Self-Assembly of Nanoparticles. *ACS Nano* **4** (7), 3591-3605 (2010).

[24] Jackson, J.D. *Classical Electrodynamics*, 3rd ed. Wiley: New York (1998).

[25] Israelachvili, J.N. *Intermolecular and Surface Forces* 3rd ed. Elsevier (2011).

[26] O'Brien, R.W., White, L.R., Electrophoretic Mobility of a Spherical Colloidal Particle. J. Chem. Soc., *Faraday Trans.* **2** (74), 1607-1626 (1978).

[27] Hermanson, K.D., Lumsdon, S.O., Williams, J.P., Kaler, E.W., and Velev, O.D. Dielectrophoretic Assembly of Electrically Functional Microwires from Nanoparticle Suspensions. *Science* **294**, 1082-1086 (2001).

[28] Gao, B., Arya, G., and Tao, A.R. Self-orienting nanocubes for the assembly of plasmonic nanojunctions. *Nat. Nanotech* **7**, 433-437 (2012).

[29] Gurunatha, K., Marvi, S., Arya, G., and Tao, A.R. Computationally Guided Assembly of Oriented Nanocubes by Modulation Grafted Polymer-Surface Interactions. *Nano Letters* **15**, 7377-7382 (2015).

[30] Laxminarayana, G.K., Rozin, M., Smith, S., and Tao, A.R. Modular, Polymer-Directed Assembly for Fabricating Metamaterials. *Faraday Discuss*. (2015).

[31] Fou, A., Onitsuka, O., Ferreira, M., Rubner, M., and Hsieh, B. Fabrication and properties of light-emitting diodes based on self-assembled multilayers of poly (phenylene vinylene). *J. Appl. Phys.* **79**, 7501-7509 (1996).

[32] Mateos, A., Cain, A., and Grunlan, J.C. Large-scale continuous immersion system for layer-by-layer deposition of flame-retardant and conductive nanocoatings on fabric. *Ind. Eng. Chem. Res.* **53**, 6409-6416 (2014).

[33] Lee, D., Rubner, M.F., and Cohen, R.E. All-nanoparticle thin-film coatings. *Nano Lett.* **6**, 2305-2312 (2006).

[34] Smith, D.R., Pendry, J.B., and Wiltshire, M.C.K. Metamaterials and Negative Refractive Index. *Science* **305**, 788-792 (2004).

[35] Landy, N.I., Sajuyigbe, S., Mock, J.J., Smith, D.R., and Padilla, W.J. Perfect Metamaterial Absorber. *Phys. Rev. Lett.* **100**, 207402 (2008).

[36] Holloway, C.L., Kuester, E.F., Gordon, J.A., O'Hara, J., Booth, J., and Smith, D.R. An Overview of the Theory and Applications of Metasurfaces: The Two-Dimensional Equivalents of Metamaterials. *IEEE Antennas and Propagation Magazine* **54** (2), 10-35 (2012).

[37] Sun, Y. and Xia, Y. Shape-controlled synthesis of gold and silver nanoparticles. *Science* **298**, 2176-2179 (2002).

[38] Angell, J.J. "Synthesis and Characterization of CdSe-ZnS Core-Shell Quantum Dots for Increased Quantum Yield." California Polytechnic State University San Luis Obispo (2011).

[39] Khon, E., Lambright, S., Smith, B., O'Connor, T., Moroz, P., Imboden, M., Diederich, G., Perez-Bolivar, C., Anzenbacher, P., and Zamkov, M. Inorganic Solids of CdSe Nanocrystals Exhibiting High Emission Quantum Yield. *Adv. Func. Mater*. **22**, 3714-3722 (2012).

[40] Near, R., Hayden, S., and El-Sayed, M. Extinction vs. absorption: which is the indicator of plasmonic field strength for silver nanocubes? *J. Phys. Chem.* **116**, 23019-23026 (2012).

[41] Rogers, B., Pennathur, S., and Adams, J. *Nanotechnology: Understanding Small Systems* 2nd ed. Taylor and Francis Group (2011).

[42] Lakowicz, J.R. *Principles of Fluorescence Spectroscopy* 3rd ed. Plenum Publishers (2006).

[43] Atwater, H.A. and Polman, A. Plasmonics for improved photovoltaic devices. *Nat. Mater.* **9**, 205-213 (2010).

[44] Li, W. and Valentine, J. Metamaterial Perfect Absorber Based Hot Electron Photodetection. *Nano Lett.* **14** (6), 3510, 3514 (2014).

[45] Zhang, B., Hendrickson, J., and Guo, J. Multispectral near perfect metamaterial absorbers using spatially multiplexed plasmon resonance metal square structures. *J. Opt. Soc. Am. B* **30**, 656-662 (2013).

[46] Moreau, A., Ciraci, C., Mock, J.J., Hill, R.T., Wang, Q., Wiley, B.J., Chilkoti, A., and Smith, D.R. Controlled-reflectance surfaces with film-coupled colloidal nanoantennas. *Nature* **492**, 86-90 (2012).

[47] Bozhevolnyi, S. and Søndergaard, T. General properties of slow-plasmon resonant nanostructures: nano-antennas and resonators. *Opt. Express* **15**, 10869-10877 (2007).

[48] Le Perchec, J., Quemerais, P., Barbara, A., and Lopez-Ros, T. Why metallic surfaces with grooves a few nanometers deep and wide may strongly absorb visible light. *Phys. Rev. Lett.* **100**, 066408 (2008).

[49] Akselrod, G.M., Argyropoulos, C., Hoang, T.B., Ciraci, C., Fang, C., Huang, J., Smith, D.R., and Mikkelsen, M.H. Probing the mechanisms of large Purcell enhancement in plasmonic nanoantennas. *Nat. Photon*. **8**, 835-840 (2014).

[50] Akselrod, G.M., Huang, J., Hoang, T.B., Bowen, P.T., Su, L., Smith, D.R., and Mikkelsen, M.H. Large-Area Metasurface Perfect Absorbers from Visible to Near-Infrared. *Adv. Mater*. **27**, 8028-8034 (2015).

[51] Esener, S. Nano 247A Optics of Biomolecules Lectures. University of California San Diego. (2015).

[52] Leatherdale, C.A., Woo, W.K., Mikulec, M.K., and Bawendi, M.G. On the Absorption Cross Section of CdSe Nanocrystal Quantum Dots. *J. Phys. Chem. B* **106**, 7619-7622 (2002).

[53] Pu, S., Yang, M., Hsu, C., Lai, C., Hsieh, C., Lin, S., Cheng, Y., and Chou, P. The Empirical Correlation Between Size and Two-Photon Absorption Cross Section of CdSe and CdTe Quantum Dots. *Small* **2** (11), 1308-1313 (2006).

[54] Butet, J., Brevet, P.-F., and Martin, O.J.F. Optical Second Harmonic Generation in Plasmonic Nanostructures: From Fundamental Principles to Advanced Applications. *ACS Nano* **9** (11), 10545-10562 (2015).

[55] Mühlschegel, P., Eisler, H.J., Martin, O.J.F., Hecht, B., and Pohl, D.W. Resonant Optical Antennas. *Science* **308**, 1607-1609 (2005).

[56] Ko, K.D., Kumar, A., Fung, K.H., Ambekar, R., Lio, G.L., Fang, N.X., and Toussaint, K.C. Nonlinear Optical Response from Arrays of Au Bowtie Nanoantennas. *Nano Lett.* **11**, 61-65 (2011).